Application of Rotating Magnetic Fields to the Travelling Heater Method Growth of GaSb and the Synthesis of CdTe

by

Jordan Douglas Roszmann

B.Eng, University of Victoria, 2006

A Thesis Submitted in Partial Fulfillment of the
Requirements for the Degree of

Master of Applied Science

in the Department of Mechanical Engineering

Application of Rotating Magnetic Fields to the Travelling Heater Method Growth of GaSb and the Synthesis of CdTe

by

Jordan Douglas Roszmann

B.Eng, University of Victoria, 2006

Supervisory Committee

Dr. Sadik Dost, Supervisor

(Department of Mechanical Engineering)

Dr. Andrew Rowe, Member

(Department of Mechanical Engineering)

Dr. Peter Oshkai, Member

(Department of Mechanical Engineering)

Supervisory Committee

Dr. Sadik Dost, Supervisor
(Department of Mechanical Engineering)

Dr. Andrew Rowe, Member
(Department of Mechanical Engineering)

Dr. Peter Oshkai, Member
(Department of Mechanical Engineering)

Abstract

Understanding and control of the flow structures in metallic fluids is important for the development of optimal crystal growth processes. One of the techniques used to control flow structures is the application of a rotating magnetic field (RMF) in the plane perpendicular to the growth direction, which induces two magnetic body force components; one in the radial direction and the other one in the circumferential direction. These two body force components alter the fluid flow in the growth system, leading to enhanced mixing, flatter growth interface, and more homogeneous crystal composition. The application of RFM was therefore considered in three separate projects: 1) the zone refining of cadmium and tellurium, 2) the synthesis of cadmium telluride (CdTe) by the travelling heater method (THM), and 3) the THM growth of gallium antimonide (GaSb).

In the zone refining of tellurium, the objective was to enhance the transport of selenium in the melt since the selenium segregation coefficient is close to unity. A magnetic field with intensity of 0.6 mT and frequency of 100 Hz was selected based on the results of earlier numerical simulations. Due to the very low electrical

conductivity of tellurium, the numerical simulations predicted a very small effect of RMF on selenium transport. The designed zone refining experiments for the tellurium system have verified this numerical simulation result. On the other hand, cadmium is an electric conductor, and thus the numerical simulations predicted a notable effect of RMF. However, experiments on the cadmium system could not be carried out because of the instability of molten zones caused by cadmium's very high thermal conductivity.

The commercial synthesis of CdTe is presently done by THM, which produces materials with much better stoichiometry than other techniques, but very slow process speeds make THM very costly. An application of RMF was considered in order to improve the speed of the process. A 1.3 mT, 0.5 Hz field was applied during the THM synthesis of CdTe. Under the experimental conditions employed, the examination of samples has shown that the application of RMF did not increase the maximum synthesis speed. The use of higher intensity RMF was not possible with the present system, but it is thought that higher fields might worsen the mixing of Cd and Te to produce non-stoichiometry.

The objective of the third project was to carry out preliminary THM growth experiments for GaSb under RMF in order to prepare a basis for future THM growth experiments aimed at reducing the cost of THM by using higher growth rates and smaller seeds with tapered ampoules. The substantially redesigned THM furnace permits rotation of the growth ampoule, better control of the experimental environment, and a stronger temperature gradient at the growth interface. Two crystals have been grown at 25 mm diameter with and without the application of a magnetic field of 0.6-mT intensity and 100-Hz frequency. These preliminary experiments have shown that the system can be used for the planned THM experiments; however, further experiments are required to attribute any effect to RMF.

Table of Contents

List of Tables

List of Figures

List of Symbols

Symbol	Description	Units
a	Axial position in zone lengths	
A_c	Cross-sectional area	m^2
B_k	Magnetic field intensity	G
C^γ	Mass concentration of solute γ	
C_l	Concentration in the liquid	
c_p	Specific heat capacity	J/kgK
C_s	Concentration in the solid	
e_k	Direction unit vectors	
e_{klm}	Permutation symbol	
E_k	Electric field	V
f	Frequency	Hz
f_k	Mechanical body force	m^2/s^2
f_k^{em}	Electromagnetic body force	N/m^3
g_k	Acceleration due to gravity	N/kg
Gr_C	Solutal Grashof number	
Gr_T	Thermal Grashof number	
H	Characteristic height	m
Ha	Hartman number	
I_k^γ	Mass flux of solute γ	kg/m^2s

J_k	Electric current density	A/m^2
k	Segregation coefficient	
k_t	Thermal conductivity	W/m^2k
n	Number of zone passes	
p	Pressure	Pa
Pr	Prandtl number	
Q	Heat flux	W
R	Characteristic radius	m
Re_ω	Magnetic Reynolds number	
T	Temperature	K
t_{kl}	Mechanical stress	Pa
t_{kl}^{em}	Electromagnetic stress	Pa
v_k	Fluid velocity	m/s
α	Thermal diffusivity	m^2/s
β_t	Thermal expansion coefficient	$1/K$
β	Solutal expansion coefficient	
δ	Skin depth	m
μ_B	Magnetic permeability	N/A^2
ν	Dynamic viscosity	m^2/s
ρ	Mass density	kg/m^3
σ_E	Electrical conductivity	S/m
ω	Angular frequency	rad/s

List of Abbreviations

Abbreviation	Meaning
CdTe	Cadmium telluride
CGL	Crystal Growth Laboratory
DC	Direct current
FCC	Face-centred cubic
GaSb	Gallium antimonide
GaInSb	Gallium indium antimonide
ICP-MS	Inductively coupled plasma mass spectrometry
PLC	Programmable logic controller
PCB	Printed circuit board
RMF	Rotating magnetic field
THM	Travelling heater method

Acknowledgements

I am grateful to Dr. Sadik Dost for the opportunity and support to pursue this thesis research. Mr. Brian Lent of the University of Victoria and Mr. Nicholas Audet and Dr. Serge Grenier of 5N Plus Inc. also helped me greatly with patient mentoring and a wealth of experience.

The projects that constitute this thesis research were funded by the Natural Sciences and Engineering Research Council of Canada, 5N Plus Inc., and The Canadian Space Agency. During my research I benefited greatly from a scholarship from the Natural Sciences and Engineering Research Council of Canada and from an Industrial Internship funded by 5N Plus Inc. and the MITACS Network of Centres of Excellence.

I would particularly like to thank my wife Andrea and our parents for their patience and support throughout my post-secondary studies.

Chapter 1

Introduction

1.1 Overview

Compound semiconductors have a greater range of properties than silicon, which makes them advantageous for devices such as infrared, X-ray or gamma ray imaging sensors and high-efficiency photovoltaic cells [1]. The synthesis of compounds can be expensive, however, and growing the bulk single crystals required for economical devices is generally more difficult for compounds than for silicon. The synthesis and growth technology for semiconducting compounds is therefore a focus for industrial and academic research.

The performance characteristics of semiconducting compounds are highly dependant on material composition. When solid material is grown from a liquid solution, however, heterogeneity in the fluid or instability of the growth interface will alter the composition of the solid product [2, 3]. Poor mass transport in the liquid solution will also reduce the solidification rate and make the process more expensive. Control of the transport phenomena in the liquid solution is therefore critical in order to accelerate growth and control the product's composition. One way to alter the flow regime in the liquid is to induce an azimuthal stirring force by applying a rotating magnetic field (RMF) [4]. In the Crystal Growth Laboratory (CGL) of the University of Victoria, RMF have been applied in the zone purification of tellurium feed

material, the travelling heater method (THM) synthesis of polycrystalline cadmium telluride (CdTe) and the THM growth of single crystal gallium antimonide (GaSb).

The THM synthesis of CdTe and the zone refining of tellurium were carried out in consultation with 5N Plus Inc. and funded through a collaborative research grant between 5N Plus and the Natural Sciences and Engineering Research Council of Canada. 5N Plus recovers base metals such as cadmium and tellurium and then zone refines them by passing molten zones through them to sweep out impurities. The purified cadmium and tellurium are then used in THM synthesis, in which a travelling zone of liquid tellurium dissolves the feed materials, and CdTe is deposited behind the travelling solution. Experimental and numerical studies were carried out to make the industrial production of CdTe less expensive. The experiments in which RMF were applied were carried out at the end of the collaborative project in order to complement the results of numerical modelling.

The application of magnetic fields to the THM growth of single crystal GaSb is the first part of a project funded through the Canadian Space Agency. Numerical models and experiments have indicated that several techniques can be used to improve the conditions in a THM growth process [3, 5, 6]. Static magnetic fields can suppress thermal convection by simulating a microgravity environment, rotating fields can improve homogeneity and axisymmetry in the solution zone, and ampoule rotation can promote thermal axisymmetry and uniformity at the growth interface. Experiments are planned to apply all three approaches to the growth of GaSb. More importantly, experiments are underway in which 10 mm diameter seed crystals are used in tapered ampoules to grow 25 mm diameter crystals. The scope of this thesis is limited, however, to the preliminary work that culminated with the growth of 25 mm diameter GaSb crystals with and without RMF.

1.2 Objectives

1. Apply RMF to the zone purification of tellurium to verify that it has no effect on the segregation of selenium as predicted by numerical modelling.

2. Compare the maximum synthesis speed and the grain size of CdTe synthesized by THM with and without the application of RMF.

3. Adapt the THM furnace and power supply for the growth of single crystal GaSb in the presence of RMF.

4. Grow GaSb crystals with and without RMF to prepare for tapered growth experiments.

1.3 Single Crystal Semiconductors

Single crystal semiconductors are the basis of the electronic metamorphosis of the world's technology since 1947. They are the materials from which transistors, diodes, light emitting diodes, optical sensors, photovoltaic cells, electrical relays, radios, integrated circuits, computers and the internet are built.

The elemental semiconductors silicon and germanium were the first to be understood and used to produce practical devices. Silicon has dominated semiconductor research and development for fifty years, and consequently silicon based devices are more easily and more economically produced than compound-based devices. The range of band gaps, lattice parameters, and optical properties achievable through the doping of elemental semiconductors is limited, however, and more flexibility must be obtained through the use of semiconducting compounds [1].

Because semiconductor devices rely on very specific electrical properties, device performance is highly sensitive to imperfections such as lattice dislocations, impurities, and local mechanical stress. All of these imperfections tend to cluster at grain boundaries, so single crystal devices perform much better than those built

Table 1.1: Elements from which compound semiconductors are formed

II	III	IV	V	VI
	Al	C	P	S
Zn	Ga	Si	As	Se
Cd	In	Ge	Sb	Te

from polycrystalline material. The growth of bulk single crystal material is a critical limiting step in the production of a large range of semiconductor devices. Refining the techniques for bulk growth of compound semiconductors is therefore critical for the economical development of improved devices such as high-efficiency photovoltaic cells.

1.4 Properties of Compound Semiconductors

Semiconductors are formed from the elements in the second to sixth columns of the periodic table, which are shown in Table 1.1. Stable covalent compounds require a full valence layer, so II-VI, III-V, and IV-IV are the three main families of compound semiconductors [1].

The elemental semiconductors, coming from group IV, have a diamond crystal structure, and most binary compound semiconductors form the very similar zincblende crystal structure, which is shown in Figure 1.1. Zincblende has the same geometry as the diamond structure, but it is formed by two interspersed face-centred cubic (FCC) sub-lattices, each consisting of atoms from one species in the binary compound. In the resulting structure, each atom is surrounded by four atoms of the opposite species arranged in a regular tetrahedron. Because of the binary nature of the zincblende structure, ternary and quaternary compounds are best interpreted as solutions of binary compounds. For example, GaInSb is a solution of InSb and GaSb wherein an FCC sub-lattice of antimony atoms is interspersed with an FCC sub-lattice composed of a solution of gallium and indium atoms.

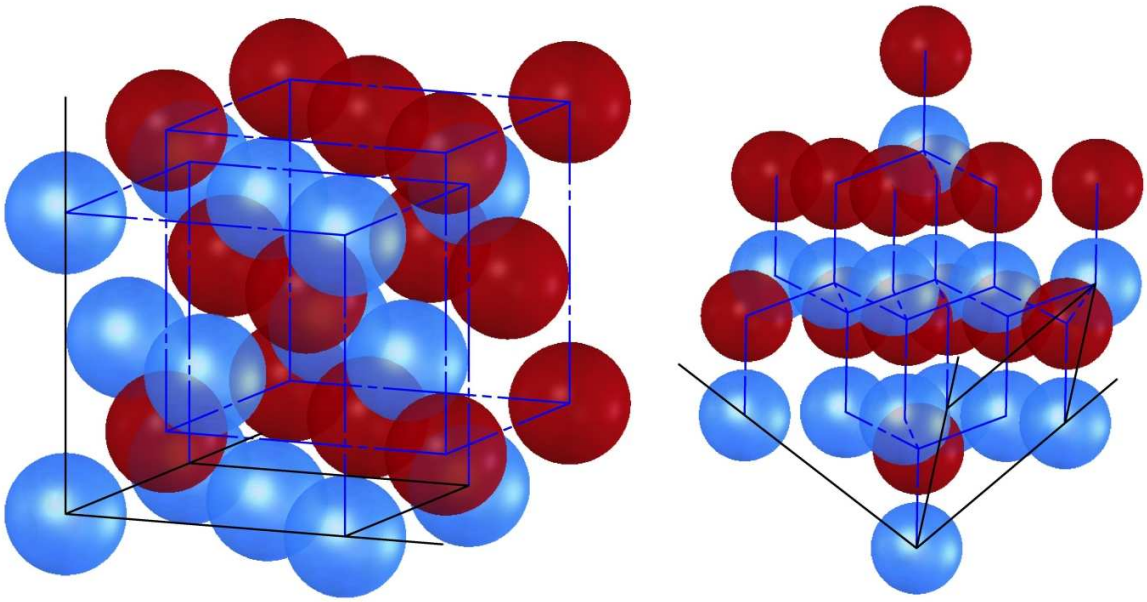

Figure 1.1: The zincblende structure oriented at left to show the FCC sub-lattices with {100} planes and obverted at right to show the overall diamond structure with horizontal {111} planes

Zincblende crystals contain many crystallographic planes, including {100} planes parallel to the walls of the FCC unit cubes and {111} planes, which appear as horizontal bands on the right side of Figure 1.1. These bands are pairs of (111)A and (111)B planes, and each plane is a layer of closely packed atoms from a single species within the binary compound. The pairing of the planes is important, because when a zinblende crystal is cut or broken along a (111) surface, the break will occur between two pairs where there are fewer atomic bonds. Therefore, a seed crystal or a wafer cut parallel to the (111) planes will always have a (111)A surface on one side and a (111)B surface on the other side. The two surfaces will have different chemical properties, and they can be distinguished by chemically etching a crystal and then determining the etch pit density on each face. When crystals are grown in the [111] direction, the seed must be oriented correctly so that growth occurs on the desired face. For example, a GaSb seed crystal used in THM growth will have an exposed layer of gallium on its (111)A side and an exposed layer of antimony on the (111)B

side. Etching the seed will produce fewer pits on the gallium terminated (111)A face, and the THM growth process is designed such that new material is deposited onto this surface.

A II-VI or III-V compound formed at low temperature will be stoichiometric, having both species in equal proportion. Such a material will have a high resistivity with the number of intrinsic charge carriers governed by its Fermi level. If the compound is slightly rich in one species, however, point defects will form including vacancies, interstitial atoms and antisites [7]. Such defects act as dopants and produce extrinsic charge carriers which lower a semiconductor's resistivity and alter the performance of devices produced from it. Crystals with more precise stoichiometry are therefore valuable, and techniques that control the stoichiometry of compounds are necessary to produce devices with consistent performance properties. Off-stoichiometry is associated with high growth temperatures because thermal vibration causes defects in the developing lattice. Growth techniques that occur at a compound's melting temperature, such as those discussed in Section 1.7.1, therefore produce more defects than vapour phase or solution growth techniques which have lower growth temperatures. The additional cost of these latter techniques can therefore be justified for some applications by the improved stoichiometry of the resulting crystals.

1.5 Gallium Antimonide

Gallium antimonide is a III-V compound semiconductor whose direct band gap, 0.72 eV, lies in the near infrared range [8].

Applications for GaSb include infrared lasers, optical sensors for the detection of water vapour or industrial gases, photodetectors for fibre-optic systems, fire detection, imaging sensors, and infrared photovoltaic absorption either as a substrate in high efficiency solar cells or alone in heat-driven thermophotovoltaic cells [8].

GaSb is also an ideal compound for basic research into fundamental semiconduc-

tor phenomena. The low vapour pressures of gallium and antimony make it relatively easy grow by the Czochralski method, described in Section 1.7.1, and chemical etches for material characterization are better established than for II-VI compounds such as CdTe. Finally, because its lattice parameter matches a wide range of other semiconducting compounds, GaSb is a useful substrate for the growth of other devices [8].

GaSb's melting point of 706^{o}C is lower than those of many compounds, but as seen in the inset of Figure 1.2, antisite solubility can still cause material to form with a gallium fraction up to 0.50004. Growing GaSb at 500^{o}C reduces the maximum amount of excess gallium in the compound by 50%.

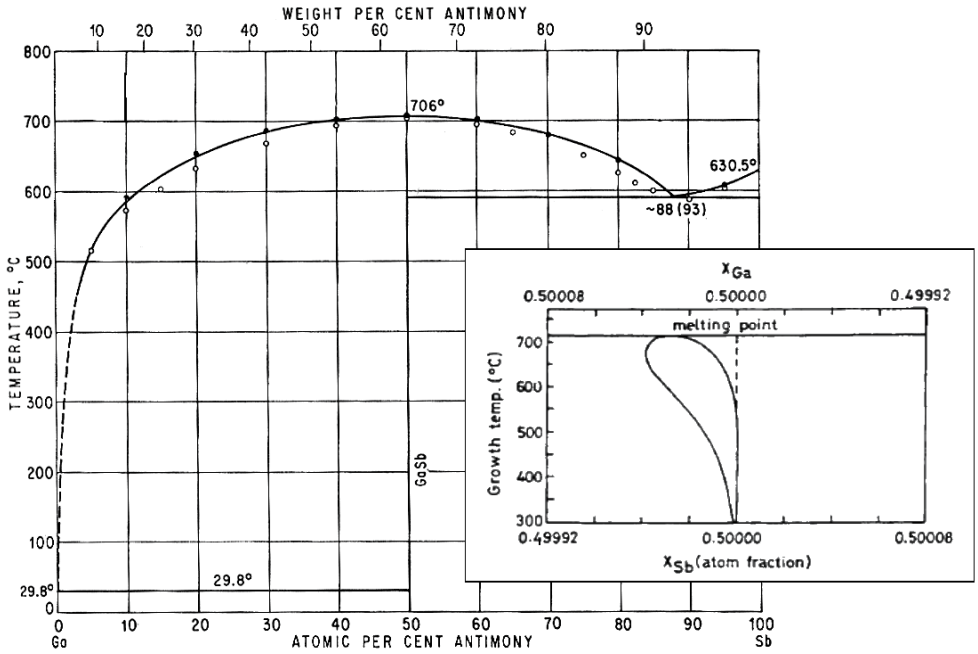

Figure 1.2: GaSb phase diagram (from [9]), Inset: High temperature existence region due to antisite solubility (from [8])

The relative densities of GaSb and its constituents can cause significant problems during crystal growth processes such as those described in §1.7. GaSb is less dense than gallium, so solid GaSb seed crystals must be secured to the bottom of the ampoule during THM growth processes. GaSb is also less dense than an equivalent

Table 1.2: Densities of gallium, antimony and GaSb

	Density (g/cm^3)	Molar Mass (g/mol)	Molar Volume (cm^3/mol)
Gallium	5.91	69.75	11.8
Antimony	6.70	121.76	18.2
GaSb (unreacted)	6.39	95.8	15.0
GaSb	5.619	95.8	17.0

mixture of unreacted gallium and antimony. For example, the third column of Table 1.2 compares the volumes of 1 mol of GaSb to an unreacted mixture with 0.5 mol of gallium and 0.5 mol of antimony. The synthesis of GaSb involves a 14% volumetric expansion. Synthesis processes must therefore be designed to allow for this melt expansion.

1.6 Cadmium Telluride

Cadmium telluride (CdTe) is a II-VI compound whose band gap of 1.45 eV and high optical absorption coefficient make it ideal for thin film solar photovoltaic cells [10]. CdTe is also chemically robust and has a relatively simple phase diagram. As a result, cheap and moderately efficient photovoltaic cells grown by sublimation and vapour deposition processes are gaining favour [11]. CdTe is also used as a high speed x-ray detector for medical, astronomical, and industrial imaging [12, 13].

Vapour deposition processes for the production of detectors and solar cells require bulk feed material that is routinely produced through THM synthesis [14]. Reducing the price of CdTe production will help to reduce the cost of emerging photovoltaic and medical imaging technologies.

1.7 Growth Techniques

1.7.1 Melt Techniques

The Czochralski method, in which a narrow seed is first dipped into and then slowly pulled out of a molten bath, is the cheapest and most widely used technique for bulk growth of semiconducting crystals. Silicon crystals more than 300 mm in diameter and 2 meters in length are grown by this method for the production of integrated circuits and solar cells. Compounds can also be grown by the Czochralski method, and commercially available GaSb crystals with diameters up to 85 mm are grown this way.

An alternate melt growth technique is to melt a sample in either a horizontal or vertical orientation and solidify it under a temperature gradient. In Bridgman growth, the heater or ingot is slowly displaced to move the temperature profile, while in gradient freezing the system is stationary and the temperature profile is moved by electronic control of the heater.

Melt growth techniques are the most common and the most economical growth techniques for bulk semiconducting compounds. As discussed in Section 1.4, however, the composition of a compound grown from the molten state is less precise than that of a compound grown at lower temperature by another method.

1.7.2 Travelling Heater Method

The THM is a solution growth technique in which a saturated solution moves through a compound ingot dissolving material at its leading dissolution interface and growing solid material at the trailing growth interface. In the THM growth of GaSb, a liquid gallium solution dissolves polycrystalline GaSb source material and deposits material onto a GaSb seed crystal.

Because of their lower growth temperature, THM grown crystals have more precise stoichiometry and fewer dislocations than those grown by the Czochralki method or

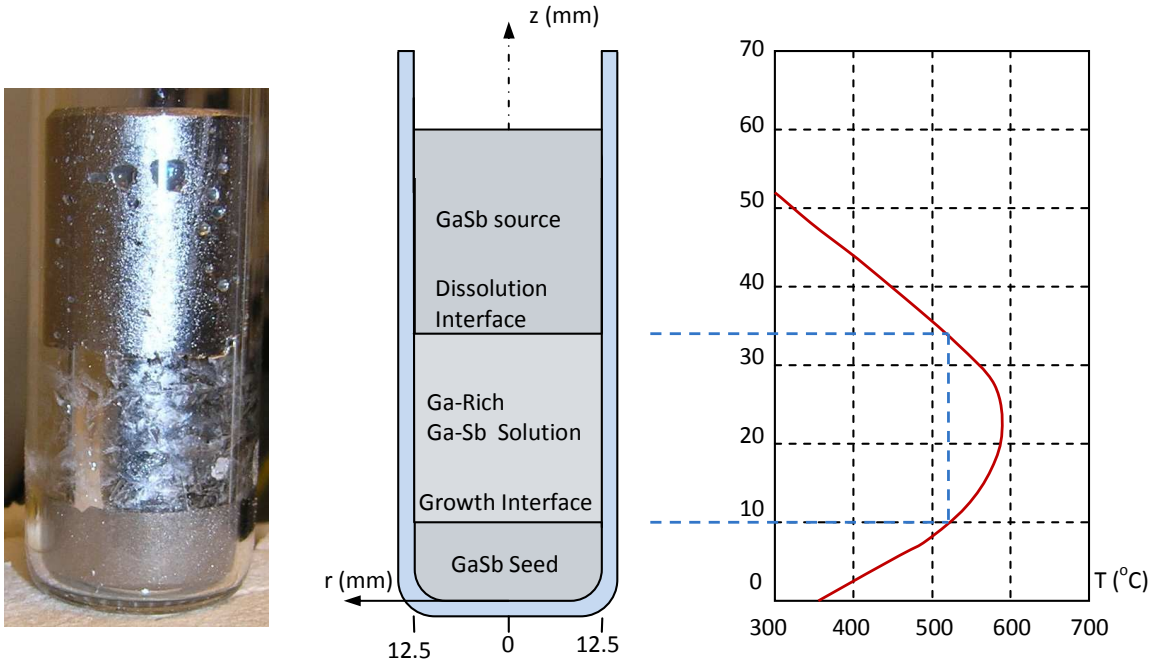

Figure 1.3: Photo and diagram of the THM growth of GaSb

gradient freezing [14]. THM is limited, however, to relatively small growth diameters and very slow growth speeds. It is therefore much more expensive than Czochralski growth which has prevented it from being used for the general commercial production of single crystals.

Unseeded THM is also used to synthesize semiconducting compounds. In the THM synthesis of CdTe, for instance, a molten tellurium solution melts cadmium and tellurium at its leading interface. CdTe precipitates out of the solution in the base of the growth ampoule, and as the temperature profile is moved, a polycrystalline ingot of CdTe is formed.

Because of the very large thermal gradients used in THM, strong convection cells tend to form in the solution zone. This strong convection may lead to an unstable growth interface and polycrystalline growth, but it can be suppressed by growing in a microgravity environment or by simulating one with a vertical magnetic field. Without convection, solutes move more slowly from the dissolution interface to the

growth interface, and it is hoped that magnetic stirring through the use of a rotating magnetic field will produce beneficial mixing of the solution zone without causing interface instability.

Accelerating the transport of solute within the THM solvent zone will allow faster growth rates and reduce the cost of production for high quality, highly stoichiometric crystals.

Chapter 2

Theory

2.1 Hydrodynamic Model of the Liquid Zones

2.1.1 Governing Thermomechanical Equations

The model that describes the electromechanical behaviour of metallic solutions is well established. The general equations are based on the balances of mass, linear momentum, moment of linear momentum, and energy; the constitutive equations for specific fluids are derived from the entropy inequality. In addition to these thermodynamic considerations, the Maxwell equations are used in cases where electromagnetic fields exist.

The Boussinesq approximation states that density changes are significant only in the body force term of the momentum equation [15]. This permits modelling of thermal convection without the complexity of full governing equations. Under these conditions, the balances of mass for the total solution and for each species yield the following continuity and mass transport equations for an incompressible Newtonian liquid.

$$v_{k,k} = 0 \tag{2.1}$$

$$\rho \frac{D(C^\gamma)}{Dt} = I^\gamma_{k,k} \tag{2.2}$$

Where the material derivative is defined as

$$\frac{D}{Dt} \equiv \frac{\partial}{\partial t} + v_k \frac{\partial}{\partial x_k} \tag{2.3}$$

The balance of momentum is given by

$$\rho \frac{D(v_k)}{Dt} = t_{kl,l} + t^{em}_{kl,l} + \rho f_k + f^{em}_k \tag{2.4a}$$

which yields the following explicit form.

$$\rho \frac{D(v_k)}{Dt} = -p_{,k} + \nu v_{k,ll} + \rho g_k \left(\beta_t (T - T_0) + \beta_c (C - C_0)\right) + f^{em}_k \tag{2.4b}$$

Equation 2.4b assumes a Newtonian fluid and neglects the electromagnetic stress, t^{em}_{kl} because the magnetic and electric fields are assumed to be uniform. f_k is the local body force due to thermal and solutal buoyancy, β_t and β_c are the thermal and solutal expansion coefficients, and f^{em}_k is the electromagnetic body force which models the effect of a magnetic field on the fluid in a solution zone.

The temperature distribution is determined from the balance of energy. It can either be combined with the momentum equation prior to solution or solved independently and iterated with the momentum balance equation. Assuming linear heat flux and neglecting the Dufour effect, the balance of energy is

$$\frac{D(T)}{Dt} = \frac{k_t}{\rho c_p} T_{,kk}. \tag{2.5}$$

2.1.2 The Electromagnetic Body Force

The effect of magnetic fields on electromagnetic materials has been modelled extensively using continuum mechanics [16]. The following equations are a summary of the established model presented in detail in [17, 18, 19].

The fluids in use are are non-magnetizable and non-polarizable. For such fluids, the body force caused by an external magnetic field is calculated from the Lorentz force equation and the generalized Ohm's law.

$$f_k^{em} = e_{klm} J_l B_m \tag{2.6a}$$

$$J_k = \sigma_E (E_k + e_{klm} v_l B_m) \tag{2.6b}$$

$$f_k^{em} = \sigma_E e_{klm} (E_l + e_{lpq} v_p B_q) B_m \tag{2.6c}$$

In these equations, the permutation symbol e_{klm} is used to express vector products. In the techniques considered, no electric field is applied to the fluid, so the magnetic field is totally applied and the electric field is entirely induced. The electric and magnetic fields are related by Faraday's law of induction.

$$e_{klm} E_{m,l} + \frac{\partial B_k}{\partial t} = 0_k \tag{2.7}$$

If the magnetic field is taken to be the curl of a vector potential, Equation 2.7 takes the form of the vector identity in Equation 2.10. The electric field therefore consists of a potential gradient and an inductive part.

$$B_k \equiv e_{klm} A_{m,l} \tag{2.8}$$

$$e_{klm}\left(E_m + \frac{\partial A_m}{\partial t}\right)_{,l} = 0_k \tag{2.9}$$

$$-e_{klm}\left(\phi_{,m}\right)_{,l} = 0_k \tag{2.10}$$

$$E_k = -\left(\phi_{,k} + \frac{\partial A_k}{\partial t}\right) \tag{2.11}$$

In the zone refining and THM projects, three pairs of magnetic coils are used to produce a magnetic field rotating at an angular frequency, ω, perpendicular to the axial direction of travel as shown in Figure 2.1. The magnetic and electric fields are defined in cylindrical coordinates, and an electric potential function is chosen that varies at the same frequency as the electric field.

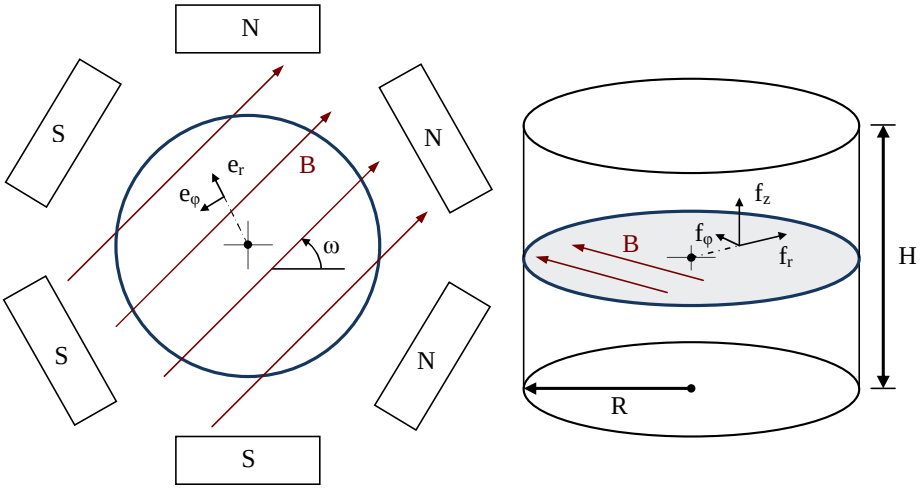

Figure 2.1: The magnetic field, **B**, rotating in the $r-\varphi$ plane and the resulting r,φ,z components of the electromagnetic body force, $\mathbf{f}^{em}$.

$$\mathbf{B} = B\left[e_r sin(\varphi - \omega t) + e_\varphi cos(\varphi - \omega t)\right] \tag{2.12a}$$

$$\mathbf{E} = -\phi_{,k}e_k + \omega r B sin(\varphi - \omega t)e_z \tag{2.12b}$$

$$\phi(r, \varphi, z, t) = \phi_1(r, z)sin(\varphi - \omega t) + \phi_2(r, z)cos(\varphi - \omega t) \tag{2.12c}$$

Substituting these definitions into Equation 2.6c, yields the three components of the magnetic body force. The force has three components, each of which has a steady part and a part that rotates at twice the frequency of the magnetic field.

$$\begin{aligned} f_r^{em} =& \frac{\sigma_E B}{2}\left(\frac{\partial \phi_1}{\partial z} - \omega r + v_\varphi B\right) sin(\varphi - 2\omega t) \\ &+ \frac{\sigma_E B}{2}\left(\frac{\partial \phi_2}{\partial z} - v_r B\right) cos(\varphi - 2\omega) \\ &+ \frac{\sigma_E B}{2}\left(\frac{\partial \phi_2}{\partial z} - v_r B\right) \end{aligned} \tag{2.13a}$$

$$\begin{aligned} f_\varphi^{em} =& \frac{\sigma_E B}{2}\left(-\frac{\partial \phi_2}{\partial z} + v_r B\right) sin(\varphi - 2\omega t) \\ &+ \frac{\sigma_E B}{2}\left(\frac{\partial \phi_1}{\partial z} - \omega r B + v_\varphi B\right) cos(\varphi - 2\omega t) \\ &- \frac{\sigma_E B}{2}\left(\frac{\partial \phi_1}{\partial z} - \omega r B + v_\varphi B\right) \end{aligned} \tag{2.13b}$$

$$\begin{aligned} f_z^{em} =& \frac{\sigma_E B}{2}\left(\frac{\varphi_1}{r} - \frac{\partial \phi_1}{\partial z}\right) sin(\varphi - 2\omega t) \\ &+ \frac{\sigma_E B}{2}\left(\frac{\varphi_2}{r}\frac{\partial \phi_2}{\partial z}\right) cos(\varphi - 2\omega t) \\ &- \frac{\sigma_E B}{2}\left(\frac{\phi_2}{r} - \frac{\partial \phi_2}{\partial r} + v_z B\right) \end{aligned} \tag{2.13c}$$

The flow induced by the Lorentz body force will also have a mean and an oscil-

lating part; however if the magnetic field rotates quickly, it is reasonable to assume that the oscillation of the fluid will be small due to inertia [17]. The net effect of the electromagnetic force can therefore be determined by taking its time average and thereby eliminating all of the sinusoidal terms in Equation 2.13.

$$f_r^{em} = \frac{\sigma_E B}{2}\left(\frac{\partial \phi_2}{\partial z} - v_r B\right) \tag{2.14a}$$

$$f_\varphi^{em} = -\frac{\sigma_E B}{2}\left(\frac{\partial \phi_1}{\partial z} - \omega r B + v_\varphi B\right) \tag{2.14b}$$

$$f_z^{em} = -\frac{\sigma_E B}{2}\left(\frac{1}{r}\frac{\partial\,(r\phi_2)}{\partial r} + v_z B\right) \tag{2.14c}$$

Numerical models commonly use Equation 2.14 when calculating the electromagnetic body force components [17, 19]. For the purpose of visualization, however, further simplifications can be made. Because the fluid velocity is assumed to be much slower than the speed of the magnetic field, terms containing velocity components may be neglected in favour of those based on ωr. Finally, because the electric field is induced from a much stronger magnetic field, terms based on the electric potential can be neglected.

$$f_r^{em} = 0 \quad , \quad f_\varphi^{em} = \frac{1}{2}\sigma_E B^2 \omega r \quad , \quad f_z^{em} = 0. \tag{2.15}$$

The rotating magnetic field therefore provides a steady azimuthal body force that is proportional to the field frequency and the square of the field intensity and which is also proportional to radial position. Rotating magnetic fields were modelled in [17] using both Equations 2.14 and 2.15, and the resultant maximum fluid velocities varied by less than 3%. The assumptions used to obtain equation 2.15 are considered

valid so long as the Hartman number is much smaller than the magnetic Reynolds number where these numbers have the following definitions [17, 20, 19].

$$Ha = BR\sqrt{\frac{\sigma_e}{\rho\nu}} \tag{2.16}$$

$$Re_\omega = R^2\frac{\omega}{\nu} \tag{2.17}$$

Several other non-dimensional numbers used to characterize electromagnetic fluid systems are the thermal and solutal Grashof numbers and the Prandtl number. These characteristic numbers have been published with the numerical models for the processes under consideration. The values obtained from these publications are listed in Table 2.1. In each process the Hartman number is much smaller than the magnetic Reynolds number, so the simplifications that yielded Equation 2.15 are valid.

$$Gr_T = \frac{\beta_t g \Delta T H^3}{\nu^2} \quad , \quad Gr_C = \frac{\beta_t g \Delta C H^3}{\nu^2} \quad , \quad Pr = \frac{\nu}{\alpha} \tag{2.18}$$

2.1.3 Skin Effects

The equations developed above assume that the magnetic field is uniform throughout the fluid volume. The skin depth of the magnetic field must therefore be greater than the radius of the ampoule or the conducting fluid will expel the magnetic field. That is, $\delta > R$. If the field rotates too quickly, its effect will be limited to a thin layer of mixing near the ampoule wall. A rotation frequency must therefore be chosen that satisfies the following restriction [17, 20].

$$\omega_B < \frac{1}{\sigma_L \mu_o R^2} \tag{2.19}$$

The electrical conductivity of the molten solvents and the permeability of free space are listed in Table 2.1. Their values can be substituted into Equation 2.19 to

Table 2.1: Characteristic properties of the experimental systems

Symbol	GaSb THM	CdTe THM	Te ZR	Units
R	12.5	12.7	21	mm
H	25	25	50 mm	
B	0.6	0.6	0.6	mT
f	100	0.5	100	Hz
ω	628	3.14	628	$rads^{-1}$
σ_E	2.5×10^6	2.5×10^5	2.5×10^5	$(\Omega m)^{-1}$
ν	1.21×10^{-7}	1.6×10^{-7}	1.6×10^{-7}	$m^2 s^{-1}$
α	3×10^{-5}	3×10^{-6}	3×10^{-6}	$m^2 s^{-1}$
ρ	5630	5620	5620	kgm^{-3}
β_t	9.85×10^{-5}	8.0×10^{-5}	8.0×10^{-5}	K^{-1}
β_c	0.084	.056	.056	K^{-1}
ΔT	50	50	50	K
ΔC	10^{-6}	10^{-6}	10^{-6}	$m^3 kg^{-1}$
μ_B	$4\pi \times 10^{-7}$	$4\pi \times 10^{-7}$	$4\pi \times 10^{-7}$	NA^{-2}
δ	0.023	1.0	0.071	m
Ha	0.454	0.127	.210	
Re_ω	8.11×10^5	3.16×10^3	1.73×10^6	
Gr_T	5.2×10^7	2.4×10^7	1.9×10^8	
Gr_c	8.8×10^2	3.4×10^2	2.7×10^3	
Pr	0.004	0.053	0.053	
Data Source	[21]	[20]	[20]	

Table 2.2: Maximum field frequency for THM solution zones

Solvent	Diameter (mm)	$\omega_{max}(rad/s)$	$f_{max}(Hz)$
Gallium	10	12,700	2,020
	25	2,040	324
	50	509	81
Tellurium	10	127,000	20,200
	25	20,400	3,240
	50	5,090	810

provide the maximum field frequencies listed in Table 2.2.

2.2 Literature Review

2.2.1 Modelling of Crystal Growth with Magnetic Fields

Ghaddar et. al. modelled the THM growth of CdTe with RMF in 1999 [20]. They found that under microgravity conditions, mixing due to RMF was able to maintain uniformity across the growth interface, but under gravitational conditions, RMF promoted complex flow structures, compositional non-uniformity, and unfavourable growth interfaces that were strongly convex toward the liquid.

At the University of Victoria, Dost et. al. have modelled the application of magnetic fields to semiconductor growth. In 1995 and 1996, a continuum model was published for electroepitaxy which is the basis of the theory discussed above [22, 23]. In 2002 Liu and Okano added a vertical static magnetic field to 2-D and 3-D models of the electroepitaxy of gallium arsenide [24]. They found that at low field strength ($Ha < 150$), convection was suppressed, but at high field strength ($Ha > 220$), unstable flow patterns formed near the ampoule wall leading to significant compositional non-uniformity across the growth interface. In 2005, models including both static fiels and RMF were published with Sheibani for liquid phase electroepitaxy and M. Yildiz and E. Yildiz for liquid phase diffusion growth [25, 15, 26].

THM growth of GaSb was modelled with Meric, Lent and Redden in 2000, and

magnetic fields were applied to the model for CdTe with Liu in 2002 [27, 28, 24, 6]. They found that a static vertical field up to 0.8 T is very beneficial for uniformity in the solution zone. At fields above 1.2 T the computation became unstable, but calculated flow and temperature fields suggested unstable transport structures and poor growth conditions. These field strengths correspond closely to the Hartman number limits found in the modelling of electroepitaxy as described above. Further modelling by Liu in 2007 showed that crucible rotation and heat extraction through the base of the crucible produced a much more favourable growth interface [5].

2.2.2 Experimental Studies

Benz, Müller et. al. have grown GaSb by THM since at least 1979. At that time, they found that for 10 mm diameter growth the best results were obtained when the zone length was between 5 mm and 8 mm and the growth interface was convex toward the liquid with a radius of curvature between 7 mm and 10 mm [29]. Later experiments focused on variation of the intensity of convection through the use of centrifuges and space-based experimentation [30, 31]. They reported a 10-fold increase in maximum growth speeds and improved interface stability through centrifugation.

In 1993, Benz and Bischopink grew 15 mm and 24 mm diameter $Al_xGa_{1-x}Sb$ by the travelling heater method at growth speeds up to 1 mm/day [32].

Salk, Benz et. al. have investigated the influence of static and rotating magnetic fields on the THM growth of CdTe through a combined numerical and experimental study [2]. Experiments were conducted in the ZONA 4 furnace on board the unmanned PHOTON 7 and PHOTON 8 space missions in 1991 and 1992. A rotating 2 mT magnetic field was applied at a frequency of 400 Hz. They found that a rotating magnetic field improved mixing in the solution zone under microgravity conditions, and turning the field off in the middle of the growth experiment resulted in supersaturation and a 1 mm distance of rapid poor quality growth which caused the crystal to crack on cooling [2]. Using ZONA 4 furnace, Senchenkov et. al. grew $Cd_xHg_{1-x}Te$

crystals with 25 mm diameter by THM under RMF of 2-6 mT and 400 Hz [3]. They found that the RMF promoted axisymmetry and allowed crystals to be grown with sufficient radial homogeneity for industrial applications.

Dold and Benz investigated the effect of RMF on metallic liquids in the late 1990's and published a review of experimental studies and numerical modelling of RMF in 1999 [4]. In particular, they observed azimuthal motion on the free surfaces of gallium melts when RMF were applied under isothermal conditions. The melts were 25 mm diameter and 50 mm tall. Under a 2 mT / 20 Hz RMF, azimuthal velocities up to 10 mm/s were measured. They also measured the temperature in gallium melts held under a temperature gradient to simulate a Bridgman growth process. 3^oC temperature fluctuations were measured due to thermal convection. The fluctuations were reduced to 0.03^oC through the application of an RMF [33].

In 2002, Michael Crowle designed and built a THM furnace for use at the University of Victoria for the growth of CdZnTe crystals under the influence of static and rotating magnetic fields [34]. His M.A.Sc. thesis included the thermal and mechanical design of the system, which became the basis for the equipment used by a Redlen Technologies in Sydney, BC. Redlen Technologies continues to use THM to grow CdZnTe crystals. In 2007 they published characterizations of crystals grown up to 56 mm long at 50 mm diameter [35]. Meanwhile, Crowle's furnace has been replaced by another THM furnace built for the CGL by Prototype Equipment Design of Esquimalt BC. This is the furnace used in the current research.

Chapter 3

Zone Refining of Tellurium

3.1 Project Overview

In a zone refining process, molten zones are passed through a solid ingot and selective transport of solutes creates a depleted region more pure than the original ingot.

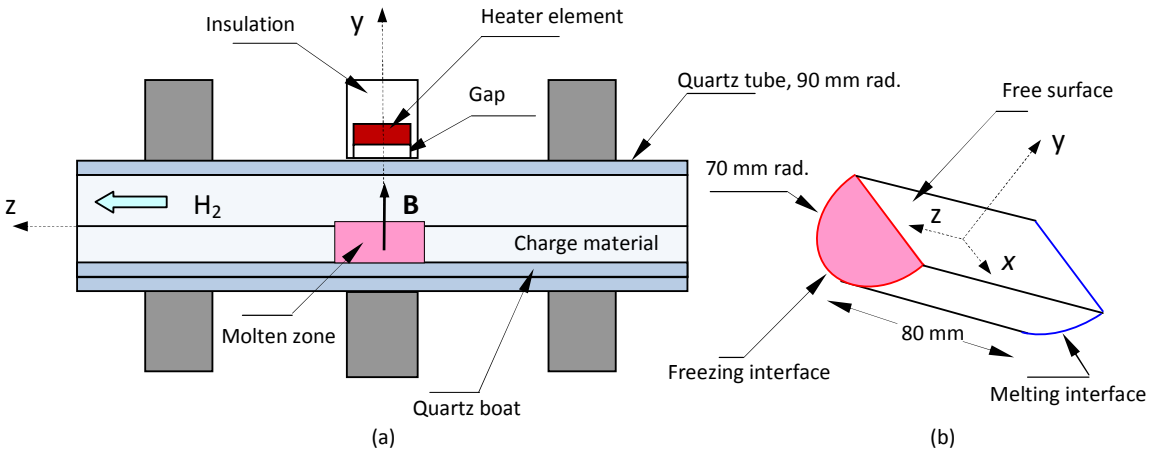

Figure 3.1: Schematic of the CGL zone refiner with a. the ingot in its quartz boat within three annular heaters and b. a molten zone with melting and freezing interfaces

A study of the zone refining of tellurium and cadmium has been carried out in collaboration with 5N Plus Inc. in order to improve the efficiency of their industrial scale systems. Numerical optimization studies were carried out at the University of Victoria by Yongcai Liu [36]. Concurrently, Jordan Haas designed an experimen-

tal apparatus to model 5N Plus's process, and he conducted experiments in order to remove selenium from tellurium ingots more efficiently [37]. The two approaches taken were to produce gaseous hydrogen selenide by exposing a fully molten ingot to a hydrogen atmosphere and to impose an applied electric current to cause the selenium to electromigrate preferentially within the molten tellurium zone. Exposure to hydrogen atmosphere did remove selenium, but the process was not efficient enough to justify its implementation in the industrial process. Electromigration failed to improve selenium transport within the tellurium ingot due to the material's low electrical conductivity [38]. In the present work, a combined numerical and experimental study investigated the effect of RMF on molten tellurium and cadmium zones. Numerical modelling by Liu found no change in either the velocity or composition fields when RMF were applied in the tellurium system [39]. In the cadmium system, the models indicated a pronounced change in both the velocity field and the impurity concentration at the solidification interface. These effects are plotted in Figures 3.2 and 3.3.

3.2 Theory of Zone Refining

3.2.1 Solute Segregation

A partially solidified solution will have solid and liquid phases in thermal equilibrium. The two phases have different compositions determined respectively from the solidus and liquidus lines of the solution's phase diagram. Such a phase diagram is shown in Figure 3.4. The solid and liquid compositions are related by the segregation coefficient, k.

$$C_s = kC_l \tag{3.1}$$

Solidification can therefore be used to change the composition of a portion of a solution. As a molten zone passes through an ingot in a zone refining process,

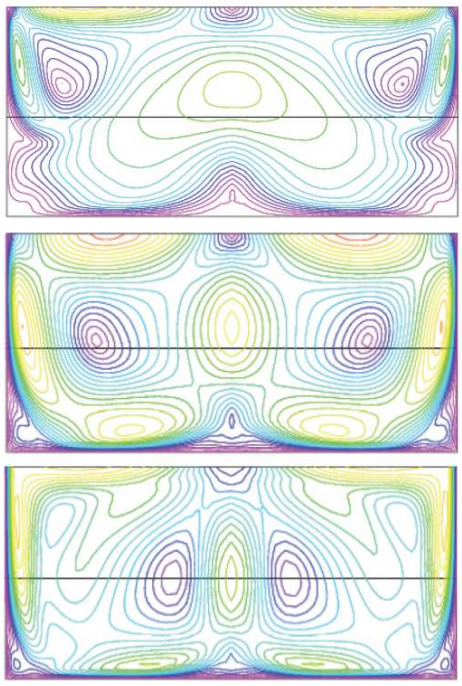

Figure 3.2: Velocity streamlines in the vertical plane along the centre of a molten cadmium zone with top: no RMF, centre: 5 mT, 20 Hz and bottom: 5mT, 90 Hz (from [39])

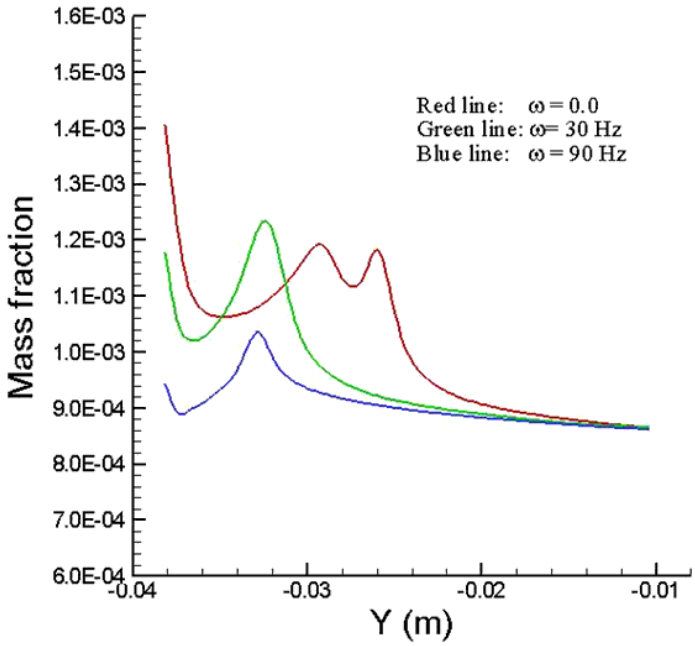

Figure 3.3: Calculated impurity concentration as a function of height on the centre line of the solidification interface of a cadmium zone under the influence of a 5 mT RMF with varing frequency, ω (from [39])

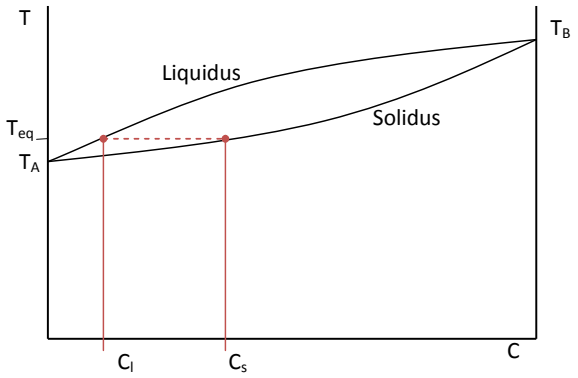

Figure 3.4: Phase diagram for a solution of two materials with melting temperatures T_A and T_B, showing the solid and liquid compositions,C_S and C_L, for a system with an equilibrium temperature T_{eq}

solutes whose segregation coefficients are smaller than one accumulate in the molten zone and are carried to the tail of the ingot. Solutes whose segregation coefficients are larger than one deplete the liquid zone and are transported forward toward the leading tip of the ingot. The closer the segregation coefficient is to unity, the more zone passes it takes to transport the solute within the ingot. In tellurium, selenium has a segregation coefficient close to unity, so selenium removal requires more zone passes than any other solute in 5N Plus processes.

The composition distribution in an ingot after n zone passes can be calculated from the following distribution [40]:

$$\frac{C_n(a)}{C_o} = 1- \\ (1-k)e^{-ka}\left[n - \sum_{s=1}^{n-1}(n-s)k^{s-1}e^{-sk}\frac{(s+a)^{s-2}}{s!}\left[a(s-1)+(1-ka)(s+1)\right]\right] \quad (3.2)$$

Where $C(a)$ is the solute mass concentration, C_o is the uniform starting concentration, a is the distance from the tip of the ingot (in zone lengths), k is the segregation coefficient and n is the number of zone passes. This equation models depletion of

solutes near the ingot tip but not accumulation near the tail, so it is valid only in the region more that n zone lengths from the ingot tail.

3.2.2 Zone Stability

Heat is injected into the liquid zone through radiation from a heating element and then passes to the solid zone by conduction. Fourier's law, evaluated at one solid-liquid interface, gives an approximate relationship between changes in the zone length and changes in the zone temperature.

$$\frac{Q}{2} = k_t A_c \frac{\partial T}{\partial x} \quad , \quad \frac{\Delta x}{\Delta T} \approx \frac{2 k_t A_c}{Q} \tag{3.3}$$

Where Q is the heater power, k_t is the thermal conductivity, and A_c is the area of the isothermal solid-liquid interface. The degree to which molten zones grow or shrink due to fluctuations in temperature is approximately proportional to the thermal conductivity of the material. Because cadmium has a thermal conductivity fifty times larger than that of tellurium, liquid cadmium zones are much more sensitive to fluctuations in heater power. Unfortunately, experiments could not carried out using cadmium in the CGL zone refiner because zones would spontaneously solidify or merge as the process progressed.

3.2.3 Transport Phenomena in the Liquid Zone

Flow in the liquid zone is governed by the mathematical model described in Chapter 2. Convective mixing in the solution zone is generally very strong due to large temperature gradients, but near the solidification interface flow velocities are slower. As can be seen in Figure 3.2, velocities are slowest in the corners at the bottom of the solid interfaces.

As the solid advances, selenium is rejected from the solidification interface and accumulates near the solid where flow velocities are small [40]. The resulting spike in impurity concentration at the solidification interface increases the concentration

in the solid and reduces the effectiveness of the zone pass. The application of an RMF is intended to improve mixing near the solidification interface, homogenize the selenium concentration across the interface, and transport more selenium into the bulk of the molten zone. Also, flows induced within the solution zone may further contribute to selenium removal by bringing more selenium into contact with the hydrogen atmosphere to form hydrogen selenide.

3.3 Experimental Study

A rotating magnetic field was applied to a tellurium zone refining process in December 2007, and the resulting ingot showed more favourable selenium segregation than those from previous electromigration experiments. Four additional experiments were therefore carried out under identical conditions with an RMF applied to the final two experiments.

The CGL zone refining apparatus, shown in Figure 3.5, consists of a horizontal quartz tube, 95 mm in diameter, fitted with sealing end caps at each end and gas ports to control the internal atmosphere. The quartz tube is surrounded by three temperature-controlled annular heaters. RMF coils surround the middle heater. The quartz tube is supported at each end by aluminum stands that are mounted to a linear actuator to translate the quartz through the heaters. The three temperature controllers and the linear actuator are controlled by a Labview virtual instrument.

In each of the four zone refining experiments, 2.5 kg of Tellurium shot was poured into a quartz boat which was placed into the quartz tube of the zone refiner. The quartz tube was repeatedly evacuated and purged with hydrogen, and hydrogen flow at 200 mL/min was maintained throughout each experiment. All three heaters were ramped to 650^oC and held for 30 minutes to completely melt the tellurium before being ramping down to 450^oC to solidify the ingot. The middle heater, fitted with RMF coils, was moved to the tip of the ingot and heated to 650^oC while the other

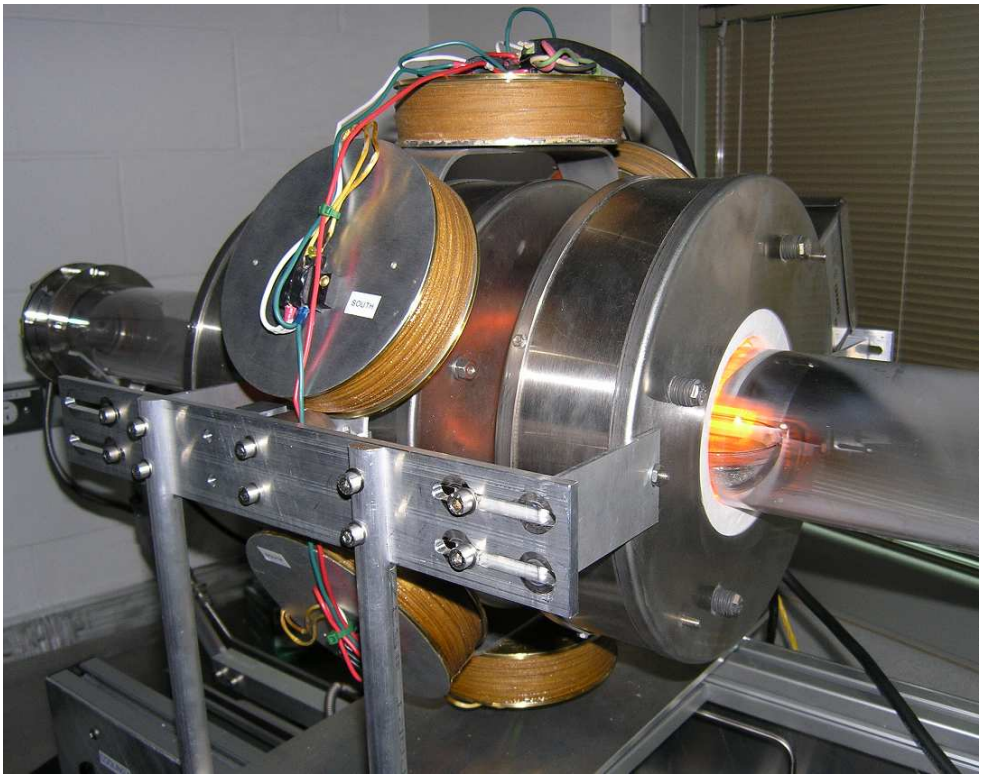

Figure 3.5: The zone refining apparatus with RMF coils installed on the middle heater

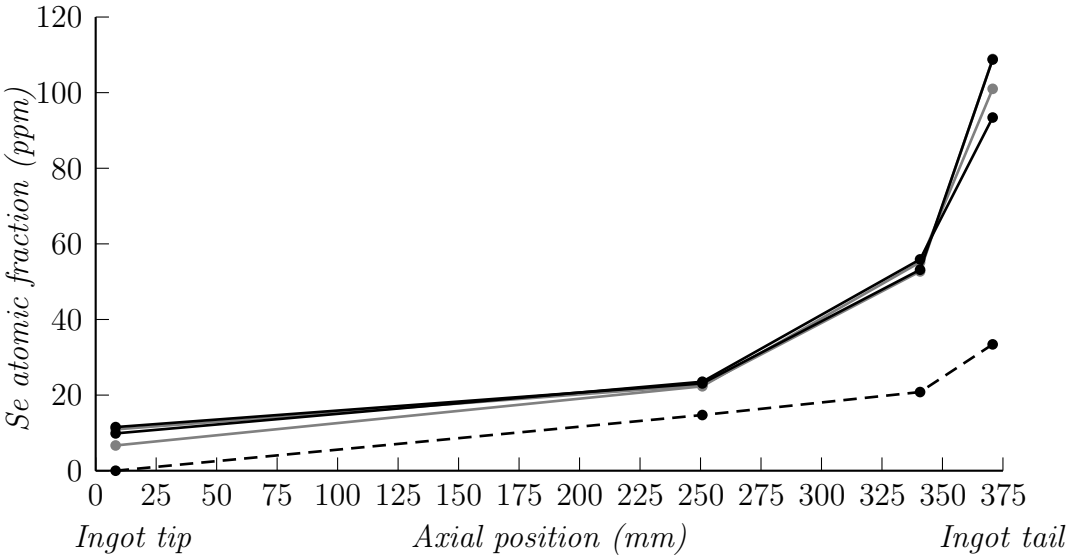

Figure 3.6: Selenium distribution in zone refined tellurium ingots. Black: with field. Grey: no field. Dashed: preliminary test.

heaters remained at 450^oC. The molten zone was passed through the ingot three times at 20 mm/hour.

After three zone passes, the ingot was cooled, removed from the zone refiner, and sliced on a diamond band saw. Four 10 mm thick slices were cut from the ingot. The slices were centred 5, 35, 125, and 365 mm from the tail of the ingot. Each slice was washed in water and methanol in an ultrasonic bath and then crushed to a powder before being packed under vacuum and shipped to 5N Plus for analysis by ICP-MS.

3.4 Results

The measured selenium concentrations measured in the resulting ingots are shown in Figure 3.4. The effective segregation coefficient for each experiment was calculated based on Equation 3.2.

The calculated effective segregation coefficients were 0.494, 0.494, 0.505, 0.474, with the latter two values calculated for experiments conducted under RMF at 0.6 mT and 100 Hz.

3.5 Discussion

Under the experimental conditions tested, RMF had no distinguishable effect on the segregation rate of selenium. This supports the result of numerical modelling that showed no effect in the tellurium system. No experiments could be conducted to support the numerical results for the cadmium system.

The field frequency of 100 Hz was chosen because it was easily achievable by the existing field generator and because it was unlikely to produce skin effects based on Table 2.2. If further experiments were to be contemplated, the frequency could be increased eight-fold according to the table. According to Equation 2.15, this would increase the magnitude of the electromagnetic body force by eight times.

Equation 3.2, which was used to calculate the effective segregation coefficient, is only valid n zone lengths away from the ingot tail where n is the number of zone passes. This is because the equation does not account for the pile up of impurities at the end of the ingot. Unfortunately, most of the samples were taken near the tail where the higher impurity concentration was more easily measured. For this reason, only the sample from each ingot's tip was used to calculate the effective segregation coefficient, and so the coefficient values obtained are only approximate values. The segregation coefficient typically used in numerical modelling is 0.8 [38]. The much more favourable coefficients calculated from these experiments are likely due to the removal of selenium to the hydrogen atmosphere, since the only concentration measurement per ingot did not permit the calculation of a concentration gradient.

Numerical studies by Liu showed that RMF was more effective in the cadmium system than in tellurium [39]. Experiments in the cadmium system were not possible, however, because stable liquid zones could not be maintained in the zone refiner. The higher thermal conductivity of cadmium causes lower temperature gradients in the ingot and makes zone length very sensitive to small changes in temperature. Cad-

mium also exhibits a much higher electrical conductivity than tellurium. According to Equation 2.15, this should produce a stronger electromagnetic body force which may allow magnetic fields to affect segregation rates in the cadmium system. The higher conductivity of cadmium does, however, encourage the onset of skin effects. If the frequency at which the skin depth is equal to the system radius is considered to be a maximum operating frequency, then Equations 2.19 and 2.15 can be combined to show that the maximum strength of the body force is independent of the fluid's electrical conductivity.

$$f_{max}^{em} = \frac{B^2}{2\mu_o R^2} r \tag{3.4}$$

The maximum force achievable is therefore no stronger in cadmium than in the tellurium system. The limit on the frequency achievable by the RMF generator, however, means that in practise stronger forces can be achieved in the cadmium system than in the tellurium system. Moreover, the numerical models suggest that the cadmium system would benefit more from the application of RMF. The collaborative project with 5N Plus Inc has concluded, but if it resumes, another attempt should be made to conduct experiments in the cadmium system.

Chapter 4

Synthesis of Cadmium Telluride

4.1 Project Overview

Polycrystalline CdTe was synthesized by THM in order to assess the impact of an RMF on grain size and interface stability. The objective of the experiments was to increase the maximum growth speed for the industrial THM furnaces used by 5N Plus Inc. In all, nineteen synthesis experiments were conducted between October 2006 and April 2007.

Each ingot produced by THM was sliced axially to allow observation of its grain structure. At low translation rates, large grains tend to grow, expand and propagate upward as the ingot precipitates. The growth interface remains stable and well defined, and very few inclusions of tellurium are entrapped within the solidified CdTe. At higher growth speeds, however, smaller grains develop and more tellurium inclusions are produced. In the final product, grain boundaries and tellurium inclusions are unfavourable, as they produce non-stoichiometry and promote the inclusion of impurities. At very high translation rates, the solidification interface becomes unstable and large amounts of tellurium are trapped within the CdTe ingot. Visual inspection of the grain size and the amount of included tellurium was used to evaluate the effect of RMF on the stability of the growth interface.

4.2 Experimental Study

Polycrystalline CdTe was synthesized from the precursor elements in 1 inch ampoules. 65 g of shotted tellurium was poured into the bottom to form a molten solution zone. Then, 120 g of cadmium was lowered into the ampoule and held upright while 170 g of shotted tellurium was poured and packed around it. Each charged ampoule was repeatedly evacuated and then filled with flowing hydrogen. It was then lowered into a hot furnace set to 800^oC and allowed to reach thermal equilibrium overnight. The ingot was then lowered at the desired growth speed.

Experiments 2 - 8 were conducted at progressively faster translation rates until large tellurium inclusions were found. The same process was repeated in experiments 9 - 12 under a 1.4 mT magnetic field rotating at 0.5 Hz until inclusions were observed at the same speeds as in the no-field experiments. After this, experiments 13 - 16 and 17 - 20 were conducted at 50 mm/day, with each series of four experiments using increasing field strengths from 0 to 1.4 mT. The grain size and the presence of visible tellurium were compared among the eight ingots in order to assess the effect of RMF on the quality of bulk material grown just below the maximum translation rate found from the previous experiments.

4.3 Results

Experiments 5 and 6 showed inclusion-free growth at 50 mm/day and significant tellurium inclusions at 75 mm/day. Experiment 8 showed significant tellurium inclusions at both 65 mm/day and 70 mm/day. Under a 1.4 mT RMF at 0.5 Hz, experiment 12 showed tellurium inclusions at both 65 mm/day and 70 mm/day. The inclusions found in experiment 12 were less significant than those of experiment 8.

The eight ingots grown subsequently at 50 mm/day showed no clear correlation between field strength and growth quality. During experiments 13 - 16, the best growth occurred at a field strength of 0.85 mT. At this strength, no voids or visible

Figure 4.1: Ingots from experiments 8 and 12. CdTe grown from the bottom at 15, 65 and 70 mm/day. Black lines indicate approximate locations of changes in growth velocity. Scale mark is 10 mm wide.

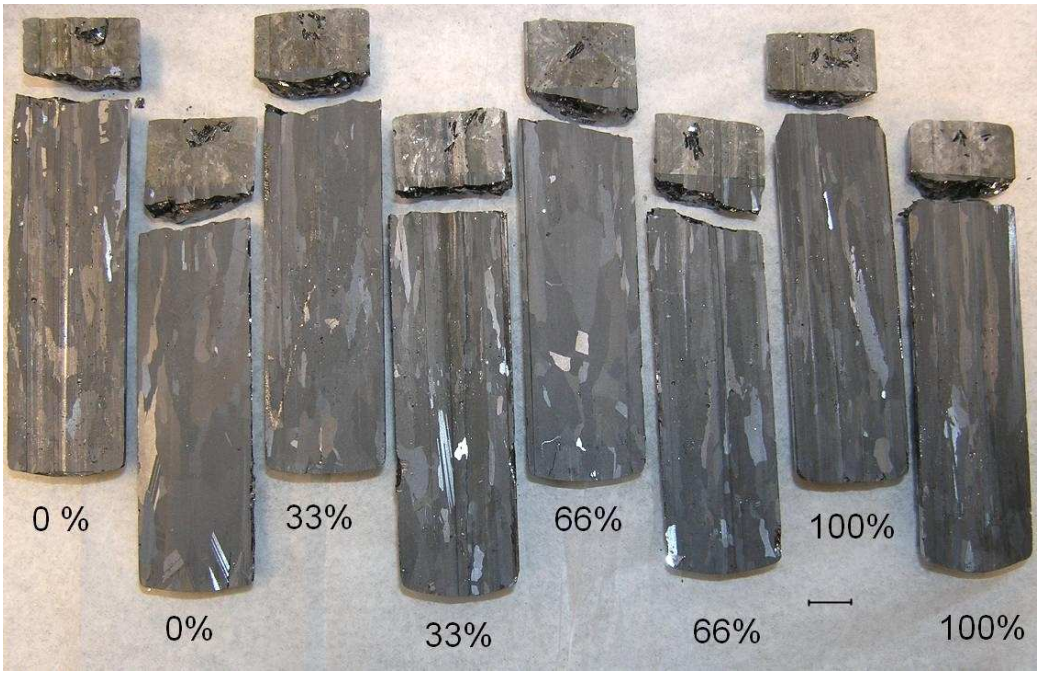

Figure 4.2: Ingots synthesized at 50 mm/day under RMF at 0.5 Hz. 100% field strength is 1.3 mT. Top row: first series, Bottom row: second series. Scale mark is 10 mm wide.

tellurium inclusions were found and large grains propagated outward as synthesis progressed. At 0.43 mT and at 1.3 mT, grain development was poorer and voids and inclusions were visible. Synthesis with no field was very poor with many small erratic grains and visible included tellurium. When the experiments were repeated in 17 - 20, however, the best grain development was found with no applied RMF, and the three ingots grown at different field strengths were of very similar quality. No correlation can be drawn between field intensity and the quality of grown crystals.

4.4 Discussion

Experiments 8 and 12 indicate that the application of an RMF under the conditions considered did not substantially increase the rate at which bulk CdTe could be synthesized by THM. There appears to be less included tellurium in the ingot grown under field; however, the onset of any tellurium inclusion at 65 mm/day indicates that the maximum growth speed could be improved by no more than 20%. The stability of THM interfaces tends to depend strongly on factors such as the strength of the temperature gradient and the stability of the system temperature. Good thermal design will have a much stronger effect on the maximum rate of synthesis than the application of an RMF to the solution zone.

The eight experiments conducted below the maximum growth rate show significant variability in the quality of synthesized material. Under these conditions, the magnetic field did not reduce the size or number of tellurium inclusions in the bulk CdTe, and it did not promote large grains or favourable grain growth. In order to produce high quality, low resistivity polycrystalline CdTe by THM, the synthesis should be conducted well below the maximum rate of translation.

A very slow field frequency was chosen to maximize the penetration depth of the field; however, it seems that this produced an electromagnetic body force that was too weak to influence the flow patterns in the solution zone. Table 2.2 shows that

the frequency could be increased as high as 3 kHz without skin effects. According to Equation 2.15, this would increase the strength of the magnetic body force by four orders of magnitude.

The collaborative research project with 5N Plus ended before further experiments or characterization could be undertaken, and the THM furnace is now being used to grow GaSb crystals. If further work were to be undertaken it could focus on several areas. The experiments conducted show only that the maximum growth rate is increased by less than 20% by the application of the magnetic field. Further experiments could determine the maximum translation rate more precisely and show whether or not the field produces a small improvement. Further, a much faster magnetic field could be employed to increase the strength of the electromagnetic body force. Finally, better characterization is required if the quality of polycrystalline material grown below the maximum translation speed is to be assessed quantitatively. Infrared transmission microscopy and scanning electron microscopy have failed to provide quantitative counts or measurements of tellurium inclusions, but laser-absorption techniques exist to measure the presence of free tellurium in CdTe powders. Such a technique would show quantitatively whether an applied magnetic field can improve the stoichiometry of bulk polycrystalline CdTe.

Chapter 5

Apparatus Design for GaSb Growth

5.1 New Rotating Endcap Mechanism

A new mechanism has been designed in order to allow rotation of the ampoule, to locate the ampoule firmly along the axis of the furnace, and to improve control of the experimental atmosphere.

As described in §2.2, numerical modelling has shown that ampoule rotation can greatly improve growth conditions, and experimental verification of this result is a goal of the GaSb growth project. The THM furnace was originally designed to allow axial translation, but it had no mechanism for rotating the ampoule. The ampoule rested on a flat pedestal, which was supported on the tip of a cone and raised or lowered by a digitally controlled stepper motor below the furnace. The ampoule was held upright only by ceramic wool wadded inside the furnace bore, and this caused several CdTe experiments to jam. Even after the wool was replaced by a tightly bored aluminum plate, the ampoule's base was free to float radially resulting in uneven heating and up to a five degree tilt from vertical. The atmosphere inside the ampoule was controlled through a Swagelok tee fitting on top of an aluminum end cap. As a hydrogen stream passed from one side of this fitting to the other, it mixed only partially with the atmosphere at the base of the ampoule from which it was separated by a long narrow channel.

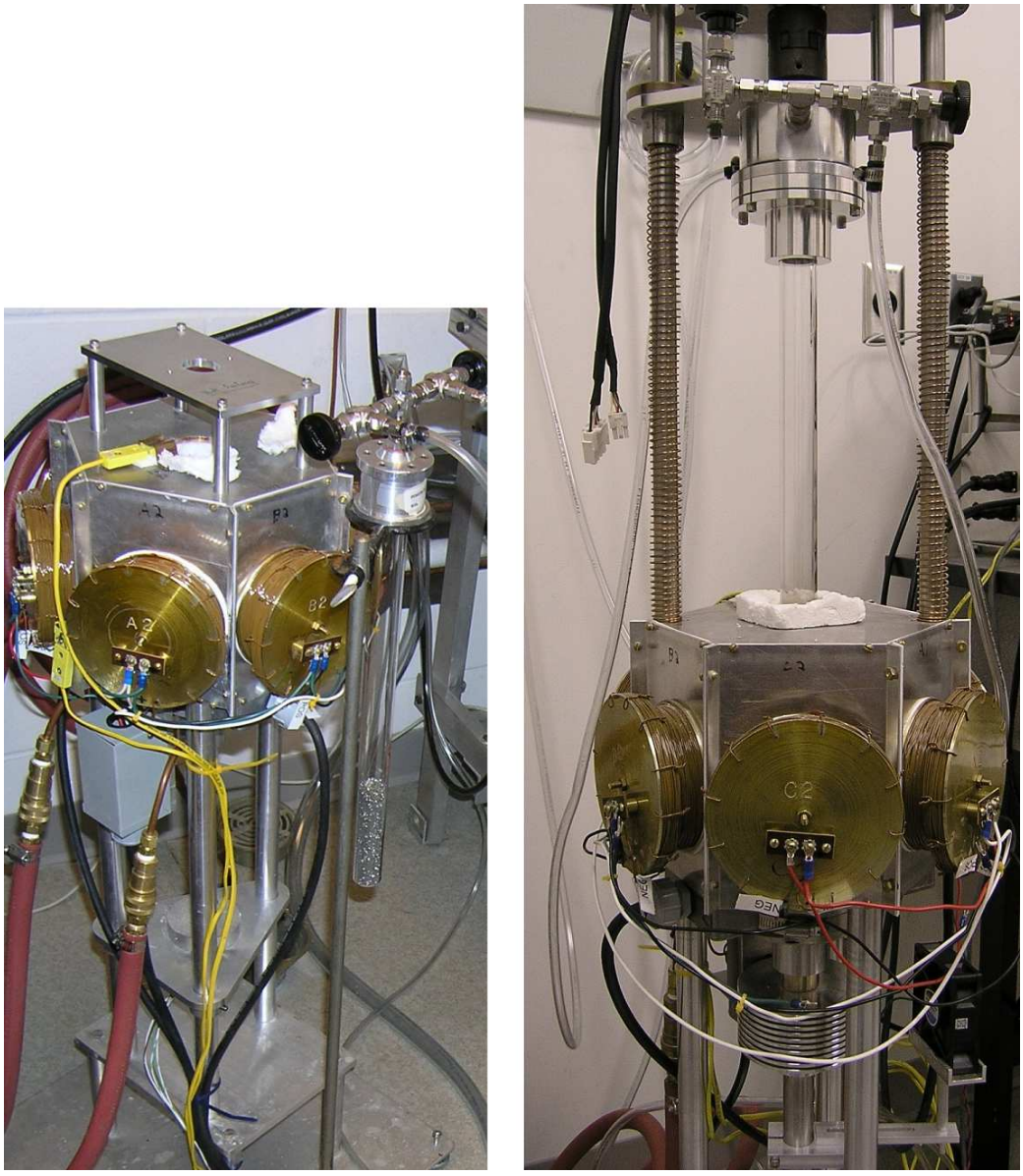

Figure 5.1: The THM furnace before and after modification for GaSb single crystal growth

The new endcap mechanism is shown in the inset of Figure 5.2. It consists of a rotating gas manifold and an electric motor mounted on cylindrical rails which are secured to the top of the furnace. The entire assembly translates freely up and down using linear ball bearings, and its 6 kg mass is partially supported by a spring wrapped around each rail. To facilitate ampoule rotation, a thrust bearing has been added below the ampoule support.

The new gas manifold is shown in Figure 5.2. The manifold is divided into two sections. The upper section allows rotation and atmosphere control while the lower section secures the ampoule. This way, the simpler lower section is easily replaced to accommodate a range of ampoule sizes without affecting the operation of the more complex upper section. The static ampoule seal is accomplished the same way as in all similar applications in the CGL. Tightening six screws squeezes a close-fitting silicone o-ring axially, and the Poisson effect causes it to press against the ampoule's outer wall. To date, such seal assemblies have been fabricated for 25 mm, 25.4 mm, and 50 mm diameter ampoules.

The upper section of the manifold consists of a rotor supported within a cylindrical housing by an angular contact ball bearing. A concentric drive shaft passes through the housing to drive the rotor and is supported by a thrust bearing. Tension in the drive shaft preloads the bearings and holds the assembly together. Torque is applied to the top of the drive shaft by a speed controlled direct current motor through a flexible coupling. An early design concept used two concentric tubes to both inject hydrogen deep into the ampoule and transmit the axial torque required for rotation. This arrangement required a very complicated end cap, however, with a minimum of three dynamic o-ring contacts. Concentric tubing was also difficult to source, so this design was abandoned in favour of a simpler end cap in which injected hydrogen mixes in a chamber above the ampoule. Two gas ports in the housing allow evacuation and atmosphere control. Sealing is accomplished by two dynamic o-ring

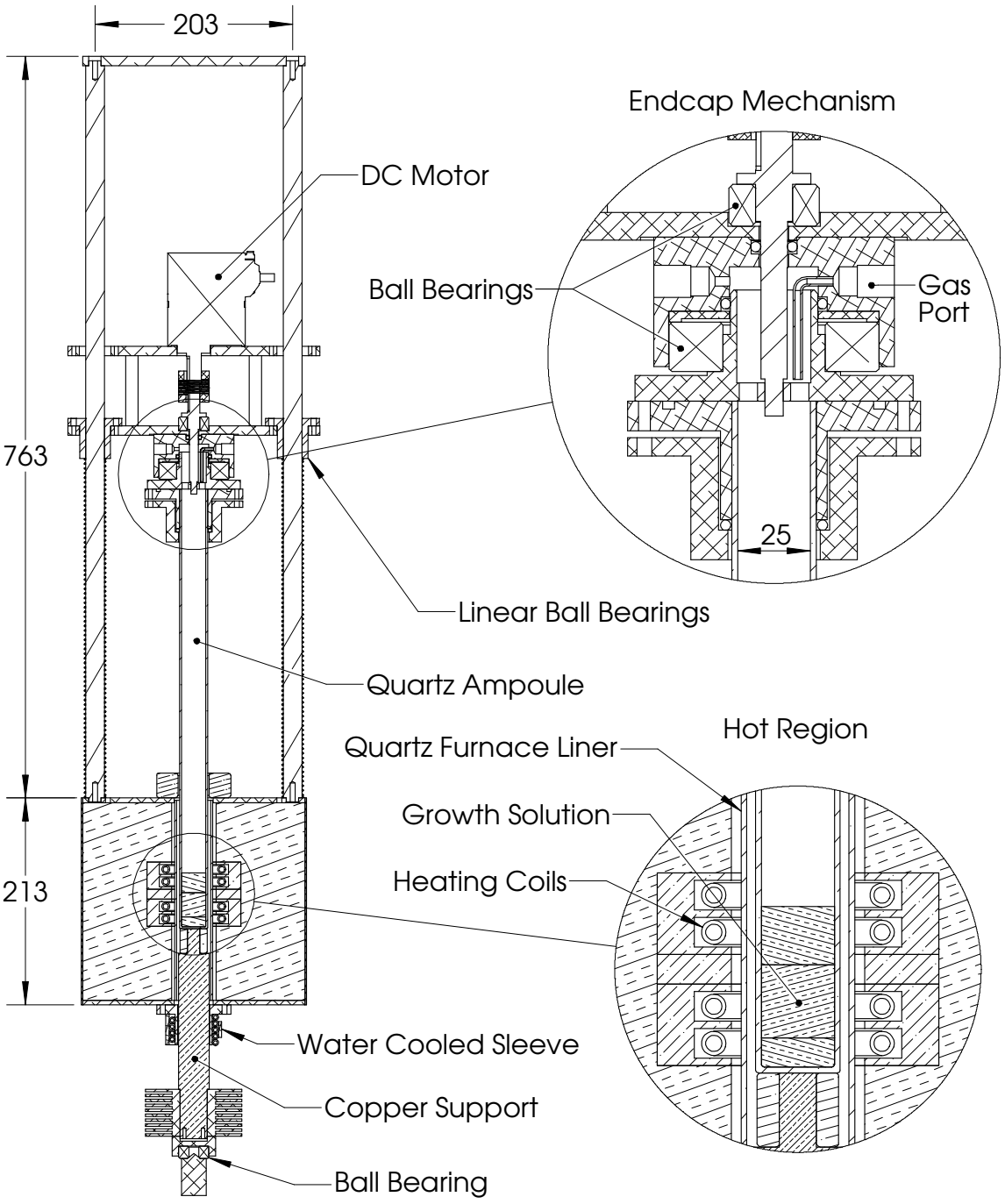

Figure 5.2: Schematic of the THM furnace after modification for the growth of GaSb crystals. Dimensions are in mm.

contacts between the housing and the drive shaft and between the housing and the rotor. The mixing chamber in the manifold is connected to the ampoule's atmosphere through six ventilation holes, and a small tube directs injected gas toward the vents to encourage mixing.

5.2 Heat Extraction

Heat extraction out of the bottom of the ampoule is critical for maintaining a strong temperature gradient at the growth interface and for causing the growth interface to be favourably convex toward the liquid. Originally, the ampoule rested on a stainless steel slug which was surrounded by insulation and sat atop of an aluminum cylinder. The aluminum column translated within a water-cooled sleeve. The stainless plug, the contact between the stainless and the aluminum and the air-gap between the aluminum and the cooling sleeve were all significant thermal resistances preventing efficient heat extraction from the bottom of the ampoule. Even the copper water lines were wrapped loosely around the cooling sleeve. Heat extraction was insufficient for the effective THM growth of single crystal GaSb.

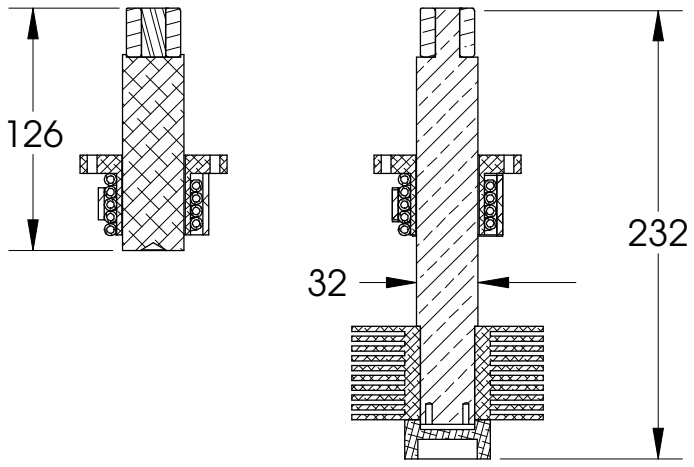

Figure 5.3: The old ampoule support and cooling sleeve and the redesigned, finned support. Dimensions are in mm.

The improved ampoule support is shown in Figure 5.3. The base of the ampoule

now rests on a single copper cylinder with a shoulder turned at the top end. This eliminates the conductive resistance and contact resistance associated with the stainless steel slug. Unlike the previous aluminum support, the copper rod extends past the cooling sleeve and is fitted with annular fins to allow direct convection to the ambient atmosphere. Thermal paste has also been added to the cooling water lines, which have been firmly clamped against the outside of the cooling sleeve in order to draw more heat through the air gap between the copper rod and the cooling sleeve.

5.3 Electrical Systems

The THM furnace was delivered with a large power supply box containing custom built DC power supplies and transistor amplifier circuits for each of the two heater elements and the RMF coils. A programmable logic controller (PLC) provided a basic user interface, read the furnace's thermocouples, and produced control signals for the heaters, the RMF, and the stepper motor driver for ampoule translation. The PLC software was unable to interface correctly with the stepper motor driver, however,so a connection was established to a notebook computer for control of the vertical translation.

The synthesis of CdTe was carried out using only the lower of the THM furnace's two heater zones. When the GaSb growth project began, however, the PLC software was found to be unable to control both temperature zones simultaneously. When the equipment manufacturer, Prototype Equipment Design, was unable to correct the error, Eurotherm 2416 temperature controllers were purchased and installed to replace the PLC. Soon thereafter, the power amplifier transistors overheated and failed repeatedly causing the furnace to operate at full power and driving its temperature well above 1000^oC. Eventually, a new power supply case was assembled containing Xantrex programmable DC power supplies controlled by the Eurotherm 2416 temperature controllers. Motor drivers for the translation stepper motor and the new DC

rotation motor were incorporated into the new case leaving only the RMF amplifiers controlled by the PLC in the original power supply case.

Once the new power supply box was operational, experiments began and work continued to repair and improve the RMF drive circuits. The original power supply consisted of a purpose-built ±80 VDC power supply and a network of power transistors driven by a control signal from the PLC. For each of the three RMF phases, two bipolar junction transistors amplified the positive half of the sinusoidal signal and another pair amplified the negative half. A resistor network on a prototype board controlled the amplifier gain. This system produced amplified signals with significant distortion and noise due to electromagnetic interference. Signal conditioning was added, but eventually significant redesign was required. This was conducted in collaboration with Kevin Jones of the Department of Electrical and Computer Engineering, and the resulting system was completed in September 2008.

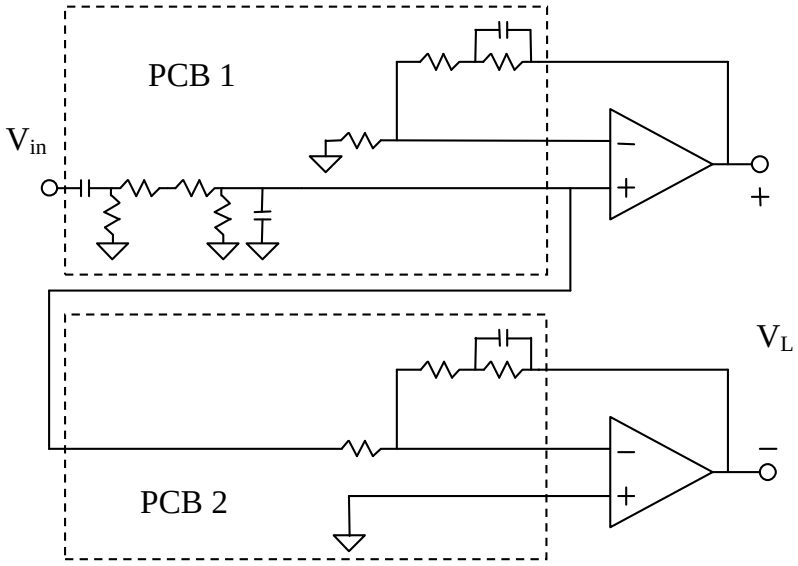

Figure 5.4: Amplifier circuit diagram for the RMF generator

In the new system, a pair of printed circuit boards containing signal conditioning circuitry receive the three phase drive signals from the PLC, and each uses three high-power operational amplifiers to produce the load current. One circuit is connected

in a non-inverting configuration and the other is inverting. The load for each phase is connected differentially between the inverting and non-inverting circuits which doubles the current achievable for a given power supply voltage. The operational amplifiers are only rated for ±30 V, so a pair of 24 VDC power supplies are used. Because of the differential operation, the voltage across the load coils can be as high as 48 V, but this is much less than the 80 V maximum of the old system. In practise, however, the voltage is never driven above 25 V because of the maximum current rating and relatively low inductance of the furnace coils. More importantly, the operational amplifiers produce a much cleaner signal than the original transistor networks which ultimately means a stronger magnetic field.

Chapter 6

THM Growth of Single Crystal GaSb

6.1 Project Overview

Single crystal THM growth of GaSb is being used to help validate the results of numerical models that have been produced to date in the CGL and to prepare for the growth of tapered crystals. In the present work, a rotating magnetic field has been applied to improve mixing in the solution zone. In the near future, a static field will be applied, and the ampoule will be rotated.

Most single crystal growth methods require high quality seed crystals. Because THM produces high quality, highly stoichiometric crystals, it is a very good candidate method for the production of seeds. One challenge with conventional THM seed production is that the production of seed material requires the consumption of a seed of the same diameter and often higher quality. To avoid this economic challenge, THM will be attempted with an expanding diameter so that a 10 mm diameter seed can be used to produce several 25 mm seeds of much greater value.

The design and fabrication of an ampoule rotation mechanism and the repair and redesign of the furnace's power supply were carried out through the fall of 2007 as described in Chapter 5. Preliminary synthesis experiments then failed because of poorly fabricated ampoules. The first source material was synthesized in December 2007 using new ampoules from a different supplier, and two growth experiments

Table 6.1: GaSb project schedule and numbered growth experiments

No.	Dates	Description
	Aug to Dec 2007	Redesign furnace, synthesize GaSb, test thermal system
1	17-Dec to 8-Jan	First attempt. Mixed single and polycrystalline growth
2	21-Jan to 6-Feb	Repeat no. 1. Again mostly polycrystalline growth
	Feb to Apr 2008	Redesign in order to enhance the thermal gradient
3	10-Apr to 21-Apr	Larger gradient, hotter furnace. Seed dissolves
4	29-Apr to 8-May	Repeat thermal tests and no. 3. Seed dissolves again
	May 2008	Construction in laboratory goes beyond schedule
5	6-Jun to 27-Jun	Cooler furnace and pre-baked seed. Seed is unwetted
6	28-Jun to 8-Jul	Higher start position than no. 5. Yields a single crystal
7	8-Jul to 19-Jul	Reuse seed from no. 6, 5 mm/day. Polycrystalline ingot
8	23-Jul to 30-Jul	Add cooling fan, difficulty wetting seed. Single crystal
9	31-Jul to 15-Aug	Use fan again. No wetting of seed, polycrystalline
	15-Aug to 8-Sept	Power outages, GaSb synthesis, thermal experiment
10	9-Sep to 21-Sep	Repeat no. 6 with recycled seed. Some polycrystallinity
11	23-Sep to 9-Oct	Repeat no. 10 with 0.6 mT 100 Hz RMF. Poor wetting
12	10-Oct to 29-Oct	Repeat no. 10 without field. Single crystal
13	30-Oct to 17-Nov	Repeat no. 11 with 0.8 mT 100 Hz RMF. Single crystal

were conducted through January 2008. These produced polycrystalline ingots, so, the heat extraction system was redesigned to increase the temperature gradient at the growth interface as described in §5.2. New thermal signatures were conducted to determine the correct furnace temperature and ampoule height under the new thermal conditions, and several experiments were prepared and scheduled for April and May 2008 during laboratory construction. In these experiments, however, the seeds floated up into the solution zones and dissolved. Experiments resumed in June 2008. A new pre-baking procedure was used to secure the seed, and the first single crystal was produced. Experiments continued through the summer in an attempt to allow faster growth by further increasing the temperature gradient, but these attempts to produce single crystals. Finally, a pair of experiments was conducted in September 2008 with and without RMF and under the same thermal conditions as the successful experiment in June. The experiments were repeated in October 2008.

6.2 Experimental Procedure

6.2.1 Material Handling

The growth experiments were conducted using gallium and GaSb, which was synthesized from gallium and antimony as described in §6.2.2. The cylindrical GaSb source was filed and etched to fit inside an ampoule of 25 mm diameter. The GaSb seeds were core-drilled from single crystal slabs 10 mm thick. The seed material was purchased from Firebird Technologies Inc. and grown by the Czochralski method. Care was taken to match the outer diameters of the source and seed to the inner diameter of the growth ampoule as closely as possible. Gallium for the solution zone was melted and poured into a mold of vinyl tubing to produce a solid cylindrical slug.

Before loading, the quartz ampoule was washed with acid as described in Table 6.2. It was then rinsed three times and filled with deionized water overnight to remove acid residue. Finally, the ampoule was rinsed with methanol and dried thoroughly.

The GaSb source ingot, gallium solvent, and GaSb seed were washed in an ultrasonic bath in three ten-minute stages using deionized water, acetone, and methanol. They were then etched according to Table 6.2 in order to remove all contaminants and oxides that might prevent the materials from wetting to each other. After the etching they were rinsed three times in deionized water, placed in an ultrasonic bath for two minutes, and finally immersed in methanol to prevent oxidation.

6.2.2 Synthesis of GaSb Source Material

Polycrystalline GaSb is required as a feed material for THM crystal growth. This material was synthesized using Bridgman and vertical gradient freezing processes which are described in §1.4. In each case, gallium and antimony were cleaned and etched and then combined in a quartz THM ampoule. The ampoule was charged with flowing hydrogen and heated to 750^oC.

Early syntheses were carried out in the THM furnace with both zones operating.

Table 6.2: Materials and etching recipes for GaSb THM growth

Material	Form	Etch Solution	Time
Gallium	Ingot	Hydrochloric acid 1 : 1 $HCl : H_20$	5 min
Antimony	Broken ingot	none	
GaSb	Ingot	Chemical polish four 1 : 1 : 2 : 3 $HF : CH_3COOH : HNO_3 : H_2O$	30 s
Quartz	Ampoule	Aqua regia 3 : 1 $HCl : HNO_3$	4 hrs
GaSb	Finished crystal	Chemical polish four 1 : 1 : 2 : 5 $HF : CH_3COOH : HNO_3 : H_2O$	3 min

As discussed in §1.5, the synthesis of GaSb involves a 14% volumetric expansion compared to the unreacted gallium and antimony. During the first syntheses, solid GaSb formed at the top of the samples, and expansion during the freezing process broke the ampoules. Unfortunately, THM furnaces are designed for large temperature gradients, so in order to keep both ends of the 60 mm GaSb sample above the melting temperature of 712^{o}C, the peak temperature in the middle of the sample had to be driven as high as 975^{o}C. The excessive temperature caused voids in the resulting ingots.

The most successful synthesis was carried out in a three zone liquid phase diffusion furnace which was designed for isothermal processes. By locating the GaSb ingot on the interface of two zones, a modest thermal gradient of approximately 1.5^{o}C/mm was established with the top surface of a 100 mm ingot held at 800^{o}C and the bottom just above the melting temperature. The liquid GaSb was cooled under the gradient to produce a solid ingot which was then cut into 20 mm lengths for use in the THM

experiments.

6.2.3 THM Growth Procedure

One disadvantage of THM growth is that it requires a complicated arrangement of starting materials in the ampoule. For GaSb, the low melting point of gallium allows relatively simple loading procedures. GaSb seeds to float in liquid gallium, however, as discussed in §1.5. This caused several experiments to fail and necessitated a two stage procedure to secure them in the bottom of the ampoule.

One gram of etched gallium was first placed at the bottom of the ampoule, and the seed was slid gently down the ampoule walls with the (111)A crystal plane facing upward. The ampoule was then charged with flowing hydrogen, and the furnace temperature was raised to 525^{o}C and held constant for at least five hours. At this temperature, the gallium became saturated with GaSb dissolved from the bottom of the seed, and it solidified and secured the seed in place. Once the system had cooled, slugs of gallium and polycrystalline GaSb were etched and added above the seed to form the solution zone and source material. The completed system was again charged with flowing hydrogen and heated to the experimental furnace temperature of 525^{o}C with the temperature profile located 5 mm higher than normal in order to prevent transient dissolution of the seed. After several hours, the profile was lowered to the starting point of the experiment. The system was allowed to settle for at least 24 hours during which time approximately 5 mm of the the 10 mm seed was dissolved. At this point, translation began at 2 mm/day and continued for up to 10 days.

6.3 Characterization Procedure

After each experiment, a 3 mm thick axial section was cut from the resulting ingot using an Isomet diamond disk saw, and its surface was polished in three stages. First, a 6 μm diamond suspension was used on a cast iron plate, then a 5 μm alumina suspension on a nylon pad polished out the pitting from the diamond, and finally a

1 μm alumina suspension produced a mirrored finish. The polished face was etched as described in Table 6.2, and the resulting etch pits were used to characterize the grown material.

A similar procedure was used at the outset of the project to differentiate the (111)A and (111)B sides of the seed material provided by Firebird Technologies Inc. The top and bottom of a piece of seed material were polished as described above and etched until dislocation etch pits were produced. The (111)A side had much fewer pits, so in experiments new material was grown on this face.

The samples were photographed through a microscope using a digital camera set to maximum telescopic zoom and infinite focus distance. A ruler was also photographed using the microscope's 10X lens, and imaging software was used to count 2100 pixels per millimetre. The frame of view was thus determined to be 1.23 mm by 0.93 mm. The frames of view for the 20X, 50X, and 100X microscope lenses were assumed to be proportional to that of the 10X lens. Scale marks a fixed number of pixels wide were added to the bitmap images before any other manipulation.

The section faces were photographed at close range, and each image's scale was determined by counting the number of pixels across either the known ingot diameter or a feature whose width could be determined from a scaled microscope photograph.

6.4 Results

The first two growth experiments were carried out between December 2007 and February 2008. In each case growth broke down very quickly to produce a polycrystalline ingot. Experiment one shows one large grain contiguous with the seed that narrows as it solidifies at the centre of the ingot. Experiment two also has a large grain, but it has a different orientation than the seed itself. In both cases, many smaller grains surround the central, large grains and gradually dominate the growth as the experiments progress. Polycrystalline GaSb has also formed around the perimeter of

the seed, where some seed material has been dissolved by gallium and where GaSb has filled the gaps between the seed and the ampoule.

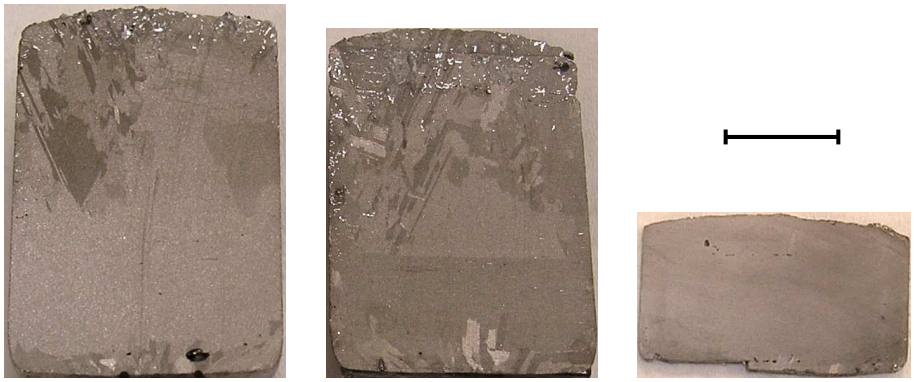

Figure 6.1: Sections cut from the ingots produced by experiments 1, 2 and 8. Scale mark is 10 mm wide.

After the thermal gradient was increased, several experiments produced ingots that were entirely polycrystalline with no remaining seed material. Several short experiments were conducted using mostly recycled material and cheaper ampoules. Two of these produced single crystals including experiment 8, which is shown in Figure 6.1 alongside the original pair of polycrystalline experiments. This ingot is a single crystal with a few very small grains visible within the larger overall lattice.

Experiments 10 and 11 were carried out using the same growth conditions as experiment 6, which had produced a single crystal. Both of these experiments produced polycrystalline ingots. Experiment 10 was grown with no applied magnetic field. Long grains propagate through the seed from its bottom up to the top of the ingot.

The section surface shown in Figure 6.2 was cut through the centre of the ingot, polished to 1 μm, and etched as described in Table 6.2. Interruptions in the crystal lattice such as dislocations or grain boundaries are preferentially etched producing triangular pits. The grain structure is therefore clearly visible macroscopically, and

Figure 6.2: Section of Experiment 10 after polishing and etching. Scale mark is 1 mm wide.

strings of individual dislocation etch pits can be seen under a microscope tracing lines of stress caused by impurities. In particular, a faint line magnified in Figure 6.3 may indicate the shape of the initial growth interface near the centre of the ingot face. The interface is slightly concave toward the liquid, but the top of the ingot is convex toward the liquid and thermal signatures all indicated convex growth interfaces. The line of dislocation pits is most likely not the initial growth interface. Rather, it could be stress caused by saw damage from the circular saw used to cut the ingot or from a deep scratch introduced during rough polishing. Unlike the grains in experiments 1 and 2 which propagated inward, narrowing the region contiguous to the seed, in experiment 10 grains propagated outward, and the central region broadens as growth progressed. This is indicative of sufficient heat extraction and appropriate growth conditions, even though the ingot itself is polycrystalline.

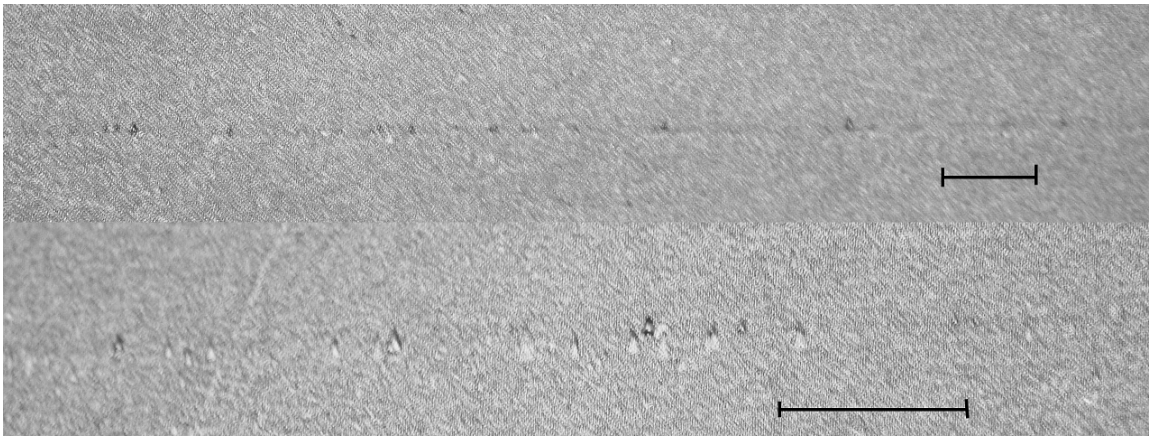

Figure 6.3: Line of dislocations on the surface of experiment 10. Both scale marks are 100 μm wide.

Experiment 11 was grown under a 0.6 mT, 100 Hz RMF. The solution did not wet fully to the seed, and the result was multiple unseeded grains grown upward above the seed, which was itself largely unaffected. The seed used for experiment 11 was recovered after an accident fractured the ingot from which it was core-drilled. As a result, the seed was not completely cylindrical and free gallium fills a region in the

lower right hand corner of Figure 6.4. It is clear from the section cut of the resulting ingot that in a few small regions growth continued from the seed, but across most of the seed's top surface, the growth solution did not wet and new grains formed unseeded above the top to the seed.

Figure 6.4: Section of Experiment 11 after polishing and etching. Scale mark is 1 mm wide.

The growth conditions of experiments 10 and 11 were repeated in experiments 12 and 13. Experiment 12, grown with no applied magnetic field, produced a single crystal. After polishing and etching, dislocation etch pits formed in regions of higher stress and are visible as white dots in Figure 6.5. After the polishing process, the section cut from the crystal cleaved into two pieces with a vertical interface. The

piece shown in 6.5 is the right piece with the cloven edge forming the left edge of the image.

Ten millimeters above the base of the crystal, a faint white line of etch pits may mark the initial growth interface. This is shown in Figure 6.6. Below this line, the dislocation etch pit density ranges from 50 to 550 dislocation pits per mm^2 with most areas approximately 150 pits / mm^2. Above the line, etch pit densities range from 90 to 700 pits / mm^2, and 500 pits / mm^2 is a typical density. This initial interface is shown under greater magnification in Figure 6.6, and typical regions of dislocations are shown in Figure 6.7. There is, however, a very large variation of etch pit densities throughout both the seed and growth regions, so the images selected cannot be considered representative.

The interface line slopes slightly upward to the right indicating a growth interface that is slightly convex toward the liquid, following approximately the same shape as the top surface of the crystal. Above this line, there are more etch pits indicating a higher dislocation density caused by greater stress in the material. In particular, many dislocations are found immediately above the line, many are located near the outside edge of the crystal, and there is a large concentration near the left edge of Figure 6.5 and near the top of the crystal. These latter dislocations are arranged in diagonal striations radiating from a small polycrystalline feature and toward a droplet of included gallium. These are shown in more detail in Figure 6.8.

Experiment 13 was carried out under 0.75 mT and 100 Hz. The resulting crystal was polished and etched and is shown in Figure 6.9. Etch pit density varies greatly in local areas, averaging approximately 250 pits / mm^2. Generally, the distribution is even across the face of the crystal. A polycrystalline feature is clearly visible, but it did not expand as growth progressed, and single crystal growth resumed eventually.

Figure 6.5: Section of Experiment 12 after polishing and etching. Scale mark is 1 mm wide.

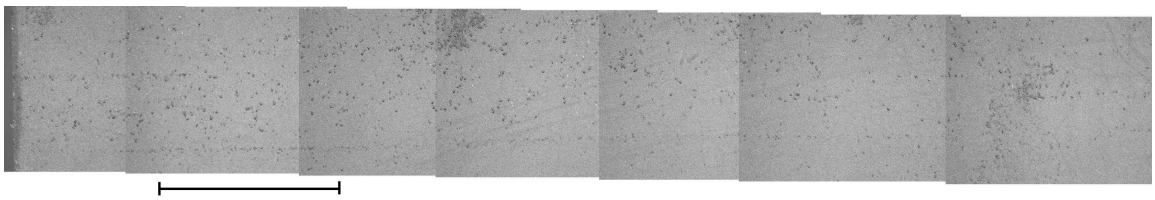

Figure 6.6: Initial growth interface near the fractured edge of Experiment 12. Scale mark is 1 mm wide.

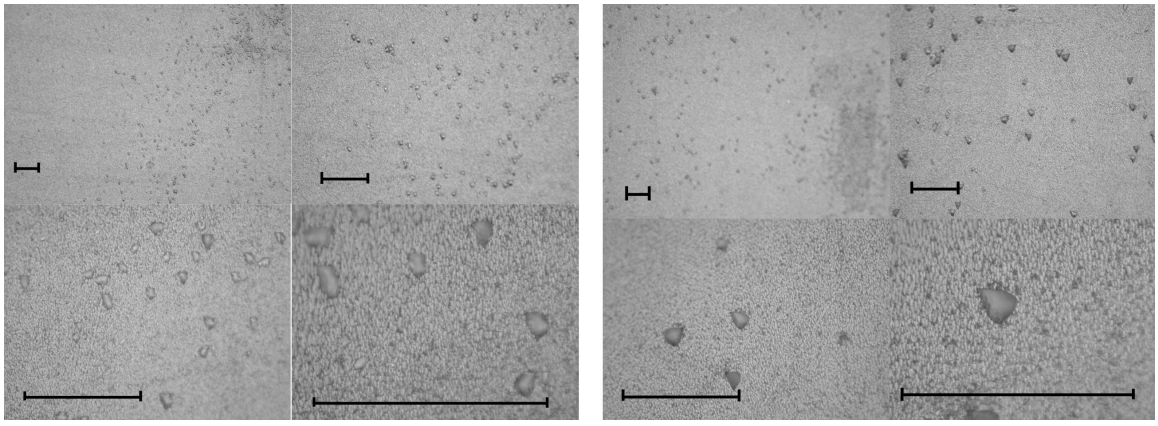

Figure 6.7: Typical etch pits at several magnifications. Left: seed, Right: growth region. Each scale mark is 100 μm wide.

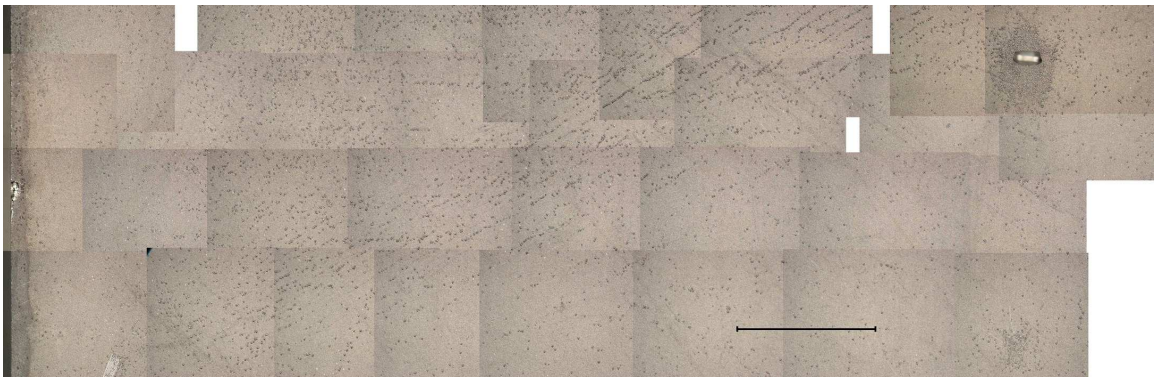

Figure 6.8: Diagonal strings of dislocation etch pits in a region of higher stress in the grown region. Scale mark is 1 mm wide.

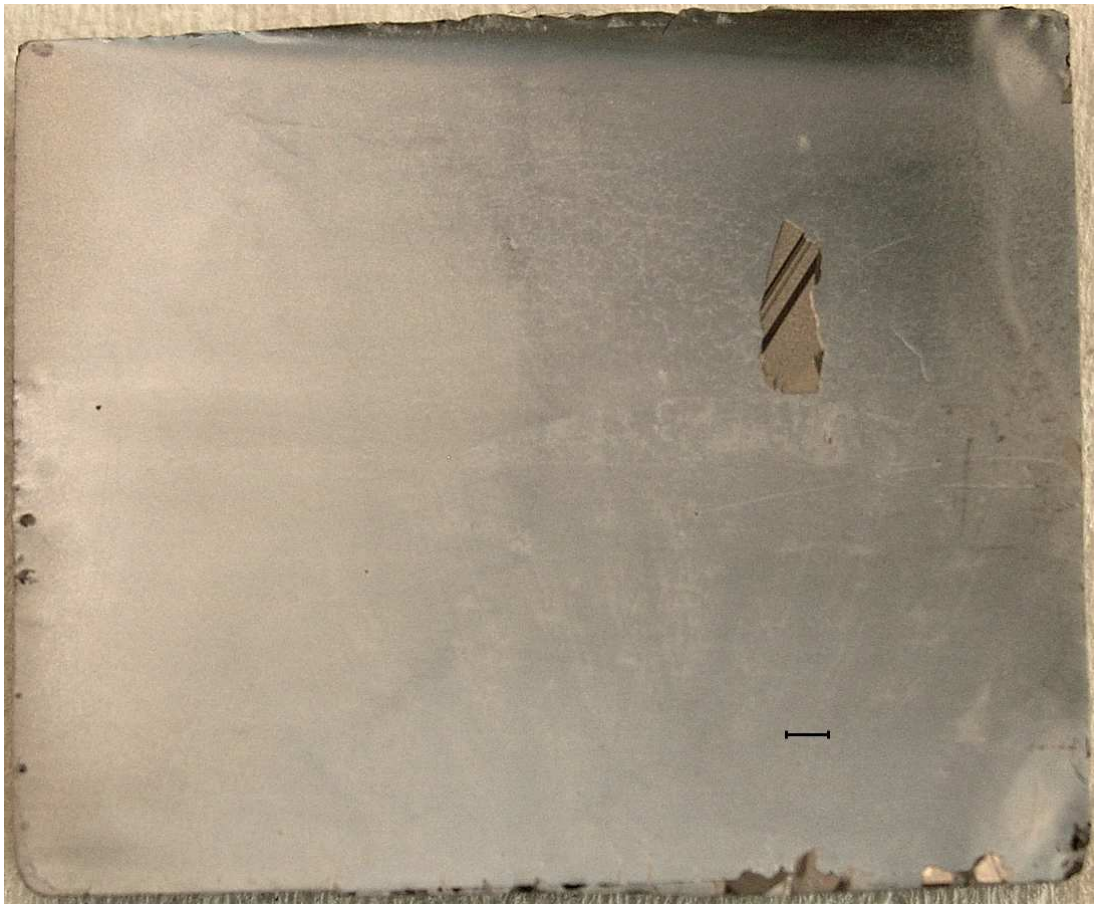

Figure 6.9: Section of Experiment 13 after polishing and etching. Scale mark is 1 mm wide.

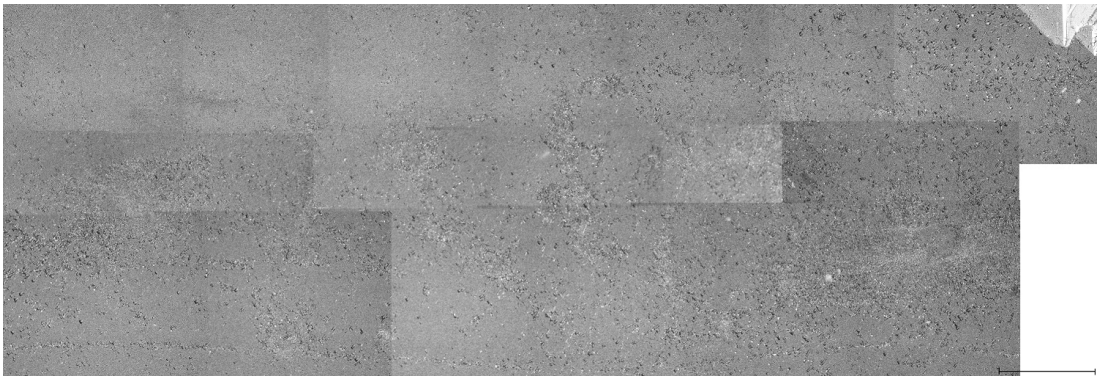

Figure 6.10: Composite photo of Experiment 13 near the polycrystalline region. Scale mark is 500 μm wide.

6.5 Discussion

Although single crystals have been grown by THM, the inconsistency of growth results has meant that no conclusions can be drawn as to the effect of rotating magnetic fields. The four most recent experiments, 10 to 13, demonstrate that the growth apparatus and material handling procedures have developed sufficiently to allow single crystal growth, but they fail to provide a consistent baseline for the investigation of growth parameters. Further experiments will be required before such investigation is possible.

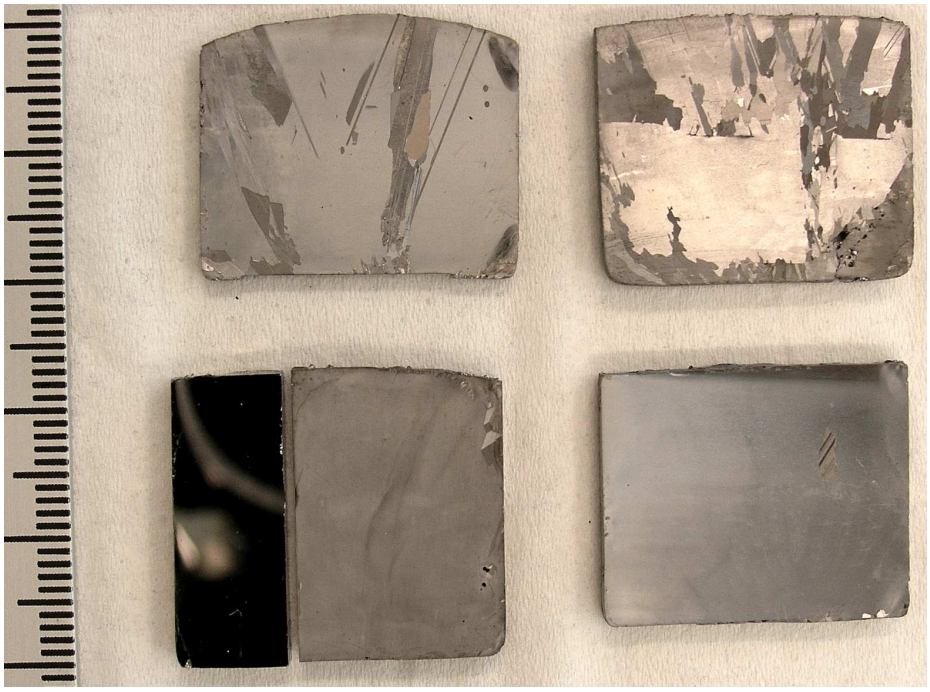

Figure 6.11: Clockwise from top left, experiments 10, 11, 13, 12. Scale is in mm.

It is noted that the two experiments conducted under RMF, those on the right in Figure 6.11, appear to have slightly flatter top surfaces, which may indicate an effect of the field. The effect is too small, and there are too few experiments, however, to clearly indicate that the field is affecting the growth conditions.

The growth interfaces in all experiments are convex toward the liquid, and grains propagate outward. These are favourable growth conditions, so the problem prevent-

ing single crystal growth in many experiments appears to be the initial condition at the onset of growth. Some grains propagate through the seed itself in experiment 10. The seed used for this experiment was recycled from a previous failed experiment, and although it appeared from the outside to be a single crystal, it is likely that grains existed within it and were exposed during the initial melt-back phase of the experiment. Growth then seeded on this polycrystalline surface and lead to a continuation of the grains through the grown ingot.

The next stage of this project is to attempt tapered growth from a 10 mm diameter seed out to a 25 mm diameter finished crystal. The success of experiments 12 and 13, and the favourable growth of experiment 10 indicate that single crystal growth is possible within the existing THM furnace as long as suitable initial conditions can be produced. It is expected that tapered growth can be established after only minimal investigation of the thermal conditions of the new system.

Chapter 7

Conclusion

7.1 Conclusions

Rotating magnetic fields have been applied in three three different processes, and the results conform with the predictions of numerical analyses.

As predicted by previous numerical studies, experimental application of RMF to the zone refining of tellurium produced no notable difference in the segregation rate of selenium. Computational modelling had suggested that RMF might improve zone refining of cadmium, but the effect would be minimal in tellurium due to its higher electrical resistivity. Stable liquid zones could not be maintained in the CGL zone refiner, however, so experiments were conducted only in the tellurium system, and their results agree with the numerical models.

In the THM synthesis of polycrystalline CdTe, the application of an RMF did not affect the maximum rate at which material could be synthesized. Under the growth conditions investigated, the quality of CdTe produced at speeds near the maximum translation rate varied too much to allow a clear correlation to be drawn between the magnitude of the applied RMF and the quality of the synthesized material.

In the single crystal growth of GaSb, the apparatus and material handling procedures have been shown to be capable of growing single crystals with and without RMF. Work has now progressed to the growth of tapered crystals from 10 mm diam-

eter seeds. This is important scientifically to investigate the transport phenomena associated with lateral growth and technologically to reduce the eventual cost of THM growth processes. This more important portion of the project can begin now that single crystal growth has been demonstrated in the CGL THM furnace.

7.2 Recommendations

Numerical studies indicate that RMF might improve the efficiency of zone refining processes in cadmium. So far, experiments have failed in the cadmium system because the molten zones have either solidified or grown too long and flooded into each other, preventing the segregation of impurities. Experiments should be carried out again in cadmium, but to prevent flooding, only one molten zone should be formed at a time. Also, cooling of the solid regions on either side of the liquid zone can be achieved using compressed air, and this will make the zone length more stable.

The RMF used in all three experimental studies were relatively weak due to the limits of the CGL's existing magnetic field generator and field coils. For future studies, stronger fields should be used to better match the conditions studied by numerical models. Several approaches may be taken to achieve this.

The THM furnace was designed to fit inside an existing superconducting solenoid in the CGL in order to permit the application of both a static magnetic field and an RMF at the same time. The furnace was therefore built from non-ferromagnetic materials, and the RMF coils are quite small. A much stronger RMF could be achieved if a static field were not required. Ferrite could then be used in the solenoid cores and for magnetic flux return paths. The CGL has already sought quotations for a system of ferrite solenoids which would be the same size as the existing static field solenoid but which would produce an RMF as large as 70 mT. Future experiments should be conducted using such a system.

An even greater field strength could be achieved if the field was held static and the

ampoule was rotated to simulate an RMF. In this case, superconducting Helmholtz coils could be used, allowing field strengths over 1 T. Ampoule rotation and the application of RMF have been studied independently by numerical models, however. Experiments should be carried out in such a way that the isolated effect of rotation and RMF may be verified. It is therefore not recommended that a static transverse magnetic field be constructed.

The THM growth furnace has been shown to be capable of growing GaSb single crystals. Further experiments should now be carried out to investigate the growth of tapered crystals using smaller seeds and to apply ampoule rotation, static magnetic fields to the growth process.

7.3 Contributions

In the course of this work, the numerical predictions that magnetic fields would have little effect on tellurium solutions were confirmed under the considered experimental conditions in the zone refining and THM systems. GaSb single crystals were grown under rotating magnetic fields. The apparatus designed for the crystal growth is now ready to undertake the novel growth of tapered crystals.

Bibliography

[1] S. Sze, *Semiconductor devices, physics and technology.* John Wiley & Sons, 1985.

[2] M.Salk, M. Fiederle, K.W.Benz, A. Senchenkob, A.V.Egorov, and D. Matioukhin, "CdTe and $CdTe_{0.9}Se_{0.1}$ crystals grown by the travelling heater method using a rotating magnetic field," *J. Crystal Growth*, vol. 138, pp. 161–167, 1994.

[3] A. Senchenkov, I. Barmin, A. Tomson, and V. Krapukhin, "Seedless THM growth of $Cd_xHg_{1-x}Te$ ($x \approx 0.2$) single crystals within rotating magnetic field," *J. Crystal Growth*, vol. 197, pp. 552–556, 1999.

[4] P. Dold and K. Benz, "Rotating magnetic fields: fluid flow and crystal growth applications," *Prog. Crystal Growth and Charact.*, vol. 38, pp. 7–38, 1999.

[5] S. Dost and Y. Liu, "Controlling the growth interface shape in the growth of CdTe single crystals by the travelling heater methdod," *C. R. Mecanique*, vol. 335, pp. 323–329, 2007.

[6] Y. Liu, S. Dost, B. Lent, and R. Redden, "A three-dimensional numerical simulation model for the growth of CdTe single crystals by the travelling heater method under magnetic field," *J. Crystal Growth*, vol. 254, pp. 285–297, 2003.

[7] P. Rudolf, "Non-stoichiometry related defects at the melt growth of semiconductor compound crystals — a review," *Cryst. Res. Technol.*, vol. 38, no. 7-8, pp. 542–554, 2003.

[8] P. S. Dutta, H. L. Bhat, and V. Kumar, "The physics and technology of gallium antimonide: An emerging optoelectronic material," *J. Appl. Phys.*, vol. 81, no. 9, 1997.

[9] M. Hansen, ed., *Constitution of binary alloys*. McGraw-Hill, 1958.

[10] C. Ferekides, U. Balasubramanian, R. Mamazza, V. Viswanathan, H. Zhao, and D. Morel, "CdTe thin film solar cells: device and technology issues," *Solar Energy*, vol. 77, pp. 823–830, 2004.

[11] G. Khrypunov, A. Romeo, F. Kurdesau, D. Bätzner, H. Zogg, and A. Tiwari, "Recent developments in evaporated CdTe solar cells," *Solar Energy Materials & Solar Cells*, vol. 90, pp. 664–677, 2006.

[12] V.Gostilo, V. Ivanov, S. Kostenko, I. Lisjutin, A. Loupilov, S. Nenonen, H. Sipila, and K. Valpas, "Technological aspects of development of pixel and strip detectors based on CdTe and CdZnTe," *Nuclear Instruments and Methods in Physics Research*, vol. A 460, pp. 27–34, 2001.

[13] K. Hori, T. Fujimoto, and K. Kawanishi, "Application of cadmium telluriude detector to high speed x-ray CT scanner," *Nuclear Instruments and Methods in Physics Research*, vol. A 380, pp. 397–401, 1996.

[14] N. Audet, B. Levicharsky, A. Zappettini, and M. Zha, "Composition study of CdTe charges synthesized by the travelling heater method," *IEEE Trans. on Nucl. Sci.*, vol. 54, pp. 782–785, 2007.

[15] M. Yildiz and S. Dost, "A continuum model for the liquid phase diffusion growth of bulk SiGe single crystals," *Int. J. Eng. Sci.*, vol. 43, pp. 1059–1080, 2005.

[16] G. A. Maugin, *Continuum mechanics of electromagnetic solids*. Elsevier, 1988.

[17] R. U. Barz, G. Gerbeth, U. Wunderwald, E. Buhrig, and Y. M. Gelfgat, "Modelling of the isothermal melt flow due to rotating magnetic fields in crystal growth," *J. Crystal Growth*, vol. 180, pp. 410–421, 1997.

[18] S. Dost and B. Lent, *Single crystal growth of semiconductors from metallic solutions*. Elsevier, 2006.

[19] E. Yildiz, "A numerical simulation study for the effect of static and rotating magnetic fields in liquid phase diffusion growth of Si_xGe_{1-x} single crystals," M.A.Sc thesis, University of Victoria, 2006.

[20] C. K. Ghaddar, C. K. Lee, S. Motakef, and D. C. Gillies, "Numerical simulation of THM growth of CdTe in presence of rotating magnetic fields (RMF)," *J. Crystal Growth*, vol. 205, pp. 97–111, 1999.

[21] H. Sheibani, Y. Liu, S. Sakai, B. Lent, and S. Dost, "The effect of applied magnetic field on the growth mechanisms of liquid phase electroepitaxy," *Int. J. Eng. Sci.*, vol. 41, pp. 401–415, 2003.

[22] S. Dost and H. A. Erbay, "A contiuum model for liquid phase electroepitaxy," *Int. J. Engng Sci.*, vol. 33, no. 10, pp. 1385–1402, 1995.

[23] S. Dost and Z. Qin, "A model for liquid phase electroepitaxial growth of ternary alloy semiconductors. part i: Theory," *J. of Applied Electromagnetics and Mechanics*, vol. 7, pp. 109–128, 1996.

[24] Y. C. Liu, Y. Okano, and S. Dost, "The effect of applied magnetic field on flow structures in liquid phase electroepitaxy — a three-dimensional simulation model," *J. Crystal Growth*, vol. 224, pp. 12–26, 2002.

[25] H. Sheibani and S. Dost, "A mathematical model for solution growth of bulk crystals under magnetic field," *Philosophical Magazine*, vol. 85, no. 33, pp. 4331–4351, 2005.

[26] E. Yildiz, S. Dost, and M. Yildiz, "A numerical simulation study for the effect of magnetic fields in liquid phase diffusion growth of SiGe single crystals," *J. Crystal Growth*, vol. 291, pp. 497–511, 2006.

[27] S. Dost, R. A. Meric, B. Lent, and R. F. Redden, "A numerical simulation model for the growth of $Ga_xIn_{1-x}Sb$ by the travelling heater method," *Transactions of the CSME*, vol. 24, no. 1B, 2000.

[28] B. Lent, S. Dost, R. Redden, and Y. Liu, "Mathematical simulation of the traveling heater method growth of ternary semiconductor materials under gravity conditions," *J. Crystal Growth*, vol. 237-239, pp. 1876–1880, 2002.

[29] K. W. Benz and G. Müller, "GaSb and InSb crystals grown by vertical and horizontal travelling heater method," *J. Crystal Growth*, vol. 46, pp. 35 – 42, 1979.

[30] G. Müller and G. Neumann, "Tenfold growth rates in the travelling heater method of GaSb crystals by forced convection on a centrifuge," *J. of Crystal Growth*, vol. 63, pp. 58–66, 1983.

[31] K.W.Benz, "Crystal growth under reduced gravity," *Prog. Crystal Growth and Charact.*, vol. 26, 1993.

[32] G. Bischopink and K.W.Benz, "THM growth of $Al_xGa_{1-x}Sb$ bulk crystals," *J. Crystal Growth*, vol. 128, pp. 470–474, 1993.

[33] P. Dold and K. Benz, "Convective temperature fluctuations in liquid gallium dependence on static and rotating magneticfields," *Crystal Res. and Technol.*, vol. 30, pp. 1135–45, 1995.

[34] M. Crowle, "Equipment designed for the growth of CdZnTe crystals by the traveling heater method under the influences of static and rotating magnetic fields," M.A.Sc thesis, University of Victoria, 2002.

[35] H. Chen, S. A. Awadalla, J. Mackenzie, R. Redden, F. Bindley, A. Bolotnikov, G. Camarda, G. Carini, and R. James, "Characterization of traveling heater method (THM) grown $Cd_{0.9}Zn_{0.1}Te$ crystals," *IEEE Trans. on Nucl. Sci.*, vol. 54, no. 4, pp. 811–816, 2007.

[36] Y. Liu, R. Moss, and S. Dost, "A computational thermal analysis for the zone-refining processes of Cd and Te," *J. Crystal Growth*, vol. 293, pp. 146–156, 2006.

[37] J. Haas, "Development of a horizontal zone refiner for optimization studies," M.A.Sc thesis, University of Victoria, 2006.

[38] J. Haas, Y. Liu, and S. Dost, "Design of a zone refiner for optimization studies," *Scientia Iranica*, vol. 14, pp. 474–485, 2007.

[39] J. Roszmann, Y. C. Liu, S. Dost, B. Lent, S. Grenier, and N. Audet, "Use of rotating magnetic field for selenium impurity transport in zone refining of tellurium and cadmium," *FDMP*, vol. 171, pp. 1–10, 2009.

[40] W. G. Pfann, *Zone melting.* John Wiley & Sons, Inc., 2nd ed., 1966.